Electrochimica Acta 371 (2021) 137837

Contents lists available at ScienceDirect

Electrochimica Acta

journal homepage: www.elsevier.com/locate/electacta

NiCu mixed metal oxide catalyst for alkaline hydrogen evolution in anion exchange membrane water electrolysis

Alaa Y. Faid[a,*], Alejandro Oyarce Barnett[b,c], Frode Seland[a], Svein Sunde[a]

[a] Department of Materials Science and Engineering, Norwegian University of Science and Technology, Trondheim, Norway
[b] SINTEF Industry, New Energy Solutions Department, Trondheim, Norway
[c] Department of Energy and Process Engineering, Norwegian University of Science and Technology, Norway

ARTICLE INFO

Article history:
Received 13 August 2020
Revised 15 January 2021
Accepted 18 January 2021
Available online 21 January 2021

Keywords:
Hydrogen evolution
Water electrolysis
Nickel based catalyst
In situ Raman
Anion exchange membrane

ABSTRACT

We report on the optimization of nickel-copper catalysts for superior performance as a cathode catalyst in anion exchange membrane (AEM) water electrolysis. The bifunctional system of NiCu mixed metal oxide (MMO) nanosheets includes Ni metallic, NiO, and CuO oxides provide rapid kinetics for the hydrogen-evolution reaction (HER) of the Volmer step. In-situ Raman spectroscopy for NiCu MMO proved that nickel hydroxide was sustained under HER conditions for at least 30,000 s, which may explain why the exceptional activity of NiCu MMO as compared to other nickel-copper catalysts is maintained over time. The activity of the NiCu MMO for the HER activity in alkaline electrolytes increased as KOH concentration raised from 0.1 M to 1 M. The NiCu MMO nanosheets showed superior stability under alkaline HER conditions for 30 h. The use of Nafion ionomer in the ink resulted in a higher HER current density as compared to inks with a Fumion anion ionomer. The maximum HER performance was achieved at a Nafion ionomer to catalyst weight ratio of 0.5. Using Ir black as the anode, the NiCu MMO cathode gave an AEM electrolyzer performance of 1.85 A/cm^2 at 2 V in 1 M KOH at 50 °C. The NiCu MMO catalyst developed here delivers AEM performance comparable to PEM water electrolysis.

1. Introduction

Efficient and cheap renewable hydrogen production from water electrolysis is a crucial challenge for a sustainable society [1,2]. Anion exchange membrane (AEM) water electrolysis aims to combine the low cost of alkaline with the advantages of proton exchange membrane (PEM) electrolyzers [3,4]. Nickel is the most active and cheapest non-noble metal catalyst reported for hydrogen evolution reaction (HER) in alkaline electrolysis [5,6]. Nickel initially shows a high HER activity, but the activity deteriorates rapidly over time due to the formation of metal hydride under HER conditions [7]. Alloying nickel with other elements such as Mo, P, S, Cu increases HER activity and stability [8]. Sluggish HER kinetics in alkaline electrolytes causes high overpotentials thus remains a challenge to develop a highly active and stable HER catalyst [9,10]. The mechanism of the HER in alkaline media is usually discussed in terms of the Volmer, Heyrovsky, and Tafel reactions [11], and a fundamental understanding of the factors influencing the rates of these steps may provide important clues for catalyst design.

NiCu has been reported as an active HER catalyst in alkaline electrolytes. NiCu catalysts have been synthesized using different processes such as freeze casting [12] electrodeposition [13] and powder metallurgy [14]. He et al. obtained a current of −10 mA/cm^2 at 117 mV with NiCu synthesized by galvanostatic deposition and with an atomic ratio of Ni to Cu equal to one [15]. Electrodeposited NiCu nanosheets exhibited enhanced HER activity with an onset potential of 48 mV vs. RHE [16]. Solmaz et al. reported that NiCu showed higher HER activity than Ni and Cu due to the roughness effect and synergistic interaction between Ni and Cu atoms [17,18]. Oshchepkov et al. found that high mass activity of $Ni_{0.95}Cu_{0.05}$/C is due to the electronic influence of Cu on Ni [19]. However, there is a deficiency in the literature of results demonstrating NiCu catalyst as a cathode in real alkaline electrolyzers.

Mixed metal oxide (Ni/NiO-transition metal oxide (TMO)) composite structures exhibit superior HER activity [20–22] NiO attracts OH_{ads} while the metallic Ni attracts H_{ads} intermediate during HER, thus lowering the free energy of the first step in the HER, viz. the formation of adsorbed hydrogen through the Volmer step of the reaction. The other TMO oxide, such as Cr_2O_3 or Fe_3O_4 appears

* Corresponding author.
E-mail address: alaa.faid@ntnu.no (A.Y. Faid).

https://doi.org/10.1016/j.electacta.2021.137837

to stabilize the composite NiO component under HER conditions [20–23]. Therefore, it is beneficial to design HER catalyst containing both a catalytic element and elements (or oxides) stabilizing mixed oxidation states for the catalytic element. Below we suggest NiCu mixed metal oxide (MMO) to catalyze the HER so that the catalyst contains both Ni (which has an affinity for H_{ad}) and NiO (which has an affinity for OH_{ad}), the simultaneous presence of these being stabilized by CuO under HER conditions.

Ionomers are frequently employed in electrochemical testing is to promote ink uniformity and coating quality [24]. The presence of the ionomer may also increase ionic conductivity and minimizes mass-transport limitations related to the diffusion of the ionic species [24]. The literature has reported that catalytic layers containing Nafion ionomer result in higher HER activity compared to catalytic layers with other anion exchange ionomers [4,21]. The activity difference has been attributed to several factors, such as ionomer head groups, and ionomer backbone chemistry [4,21]. However, tuning ionomer to catalyst ratio is required for optimum catalyst utilization [25]. Not only its activity and stability but also the interaction of NiCu metal mixed oxide catalyst with ionomers and effects of an aqueous electrolyte, is therefore also important if this catalyst is to play a role in upscaling to AEM water electrolyzer devices, preferably including not only experiments in aqueous cells but also electrolyzer testing.

In this work, we investigate the HER activity of various nickel-copper catalysts such as NiCu alloy, NiCu oxide, and NiCu mixed metal oxide (MMO) synthesized by chemical reduction. As we will show below, NiCu MMO shows an exceptional HER activity in alkaline media. In situ Raman spectroscopy under HER conditions was carried out to investigate the state of copper and nickel species present and how these states vary over time for various nickel copper catalysts and correlate this with their activity for the HER. The electrochemical activity of NiCu MMO was further optimized in terms of the type of ionomer binder, KOH concentration in the aqueous electrolyte, and the ionomer to carbon ratio. An AEM water electrolyzer based on membrane electrode assembly (MEA) of NiCu MMO at the cathode and Ir black at the anode was fabricated, tested, and compared to Pt/Ir MEA. The NiCu MMO/Ir MEA shows comparable performance to Pt/Ir MEA which indicates that it could replace scarce and expensive Pt catalyst.

2. Experimental

2.1. Catalyst synthesis

NiCu alloy and NiCu oxide were synthesized by mixing 10 mmol of nickel nitrate hexahydrate $Ni(NO_3)_2.6H_2O$ (97.0%, Sigma Aldrich) and 10 mmol Copper(II) sulfate pentahydrate (98.0%, Sigma Aldrich) in 500 ml water (18.2 MΩ cm, 3 ppb TOC, Milli-Q ultrapure water). The precursor mixture was stirred for 15 min at 750 rpm. 200 ml of 0.15 M $NaBH_4$ (98%, Sigma Aldrich) was added dropwise while bubbles were observed. The solution mixture was stirred for another 1 hour to ensure the complete chemical reduction of precursors. The resulting precipitate was centrifuged 5 times at 8000 rpm for 6 min and cleaned with water and ethanol three times. The produced precipitate was dried in a vacuum oven at 80 °C overnight. The dried powder was annealed in an air atmosphere to obtain NiCu oxide or 5%H_2/Ar to obtain NiCu alloy. The annealing was done at 500 °C for 6 h with a ramping rate of 10 °C/min.

In order to make NiCu MMO, 100 ml of 1 M Na_2CO_3 (≥99.5%, Sigma-Aldrich) were added to nickel-copper precursors solution until the solution became milky and pH reached 10. The mixture was then stirred for another 15 min, followed by the addition of $NaBH_4$ dropwise. The produced catalyst was subjected to the same procedure for cleaning and drying as above. The dried powder was annealed in 5%H_2/Ar atmosphere at 500 °C for 6 h with a ramping rate of 10 °C/min.

For catalyst supported on carbon, Ketjen black EC-600JD (AkzoNobel) was dispersed in the precursors' solution mixture to get (60 wt% catalyst supported on carbon) and stirred for another 1 hour before adding $NaBH_4$ and complete the chemical reduction step.

2.2. Structural and electrochemical characterization

Scanning electron microscopy (SEM, Carl Zeiss supra 55) and energy dispersive X-ray (EDX) spectroscopy in the SEM device were used to study the morphology and elemental composition of catalysts. The catalyst morphology was further studied using Hitachi S-5500 via scanning transmission electron microscopy (STEM) mode. Bruker D8 A25 DaVinci X-ray device (Cu-Kα radiation with a wavelength of 1.5425 Å) was used to examine the crystalline characteristics of catalysts. X-ray diffraction (XRD) patterns were taken between 15 [2θ] and 75 [2θ] using a step size of 0.3 [2θ]. WITec alpha300 R Confocal Raman device with a 532 nm laser was used to collect the Raman vibrational characterstics of catalyst powders. X-ray photoelectron spectroscopy (XPS) was done via an Axis Ultra DLD instrument (Kratos Analytical) equipped with Al X-ray monochromatic source.

Electrochemical investigation of the catalysts was carried out in a three-electrode cell using a rotating disk electrode (Pine Research,) with an (Ivium-n-Stat) potentiostat. Carbon paper (Toray 090, Fuel cell store) was used as the counter-electrode while Hg/HgO electrode (Pine Research) was served as the reference electrode. The working electrode was catalyst deposited on glassy carbon (GC) electrodes (5 mm diameter, Pine Research). The GC electrode was polished using alumina suspension (5 and 0.05 μm, Allied High-Tech Products, Inc.) on polishing pads. The GC electrode was then washed, sonicated in 1 M KOH for 5 min, and finally rinsed with water. The catalyst ink was prepared by dispersing 10 mg catalyst powder in 1.0 mL of a solution [500 μL water, 500 μL isopropanol]. The ionomer used was either Nafion (5 wt%, Alfa Aesar) or anion exchange ionomer Fumion FAA-3 (10 wt% fumatech) with an ionomer to catalyst weight ratio of 0.2. The Nafion ionomer to catalyst weight ratio in the ink was then optimized from a selection of weight ratios equal to 0.1, 0.3, 0.5, 0.7, and 0.9. The ink was then sonicated for 30 min in an ice bath. Catalyst loading on the GC surface was kept 250 μg/cm^2.

The catalyst ink was spin-coated on a GC electrode turned upside down and rotated to assure a homogenous catalyst distribution. A water drop was deposited on the electrode before immersed in the electrolyte to prevent air bubbles from forming at the electrode surface. All the electrochemical measurements were conducted in N_2-saturated 1 M KOH electrolyte at room temperature (20 ± 2). The electrolyte was purged for 30 min with N_2 gas before using and during the experiment to remove any dissolved gasses during electrochemical measurements. The electrolyte was prepared by using KOH (Sigma Aldrich, 85%), and water (18.2 MΩ cm, Milli-Q® Integral ultrapure water). The electrolyte was purified according to the procedure reported by Trotochaud et al. [26].

The working electrode underwent electrochemical activation by cycling between −0.8 to −1.5 V vs Hg/HgO at a scan rate of 100 mV/s for 50 cycles. The linear sweep voltammetry (LSV) polarization curves were recorded in a potential range of −0.8 to −1.5 V vs. Hg/HgO at 1 mV/s sweep rate under continuous stirring at 1600 rpm to avoid the accumulation of gas bubbles over the GC electrode. The electrochemical impedance spectroscopy (EIS) measurements were collected at specific overpotentials (−100 to −250 mV) in a frequency range of 0.1 − 10^5 Hz with an amplitude of 10 mV alternative current (AC) perturbation. In this work, ohmic resistance (IR) drop was compensated at 85% of high-frequency

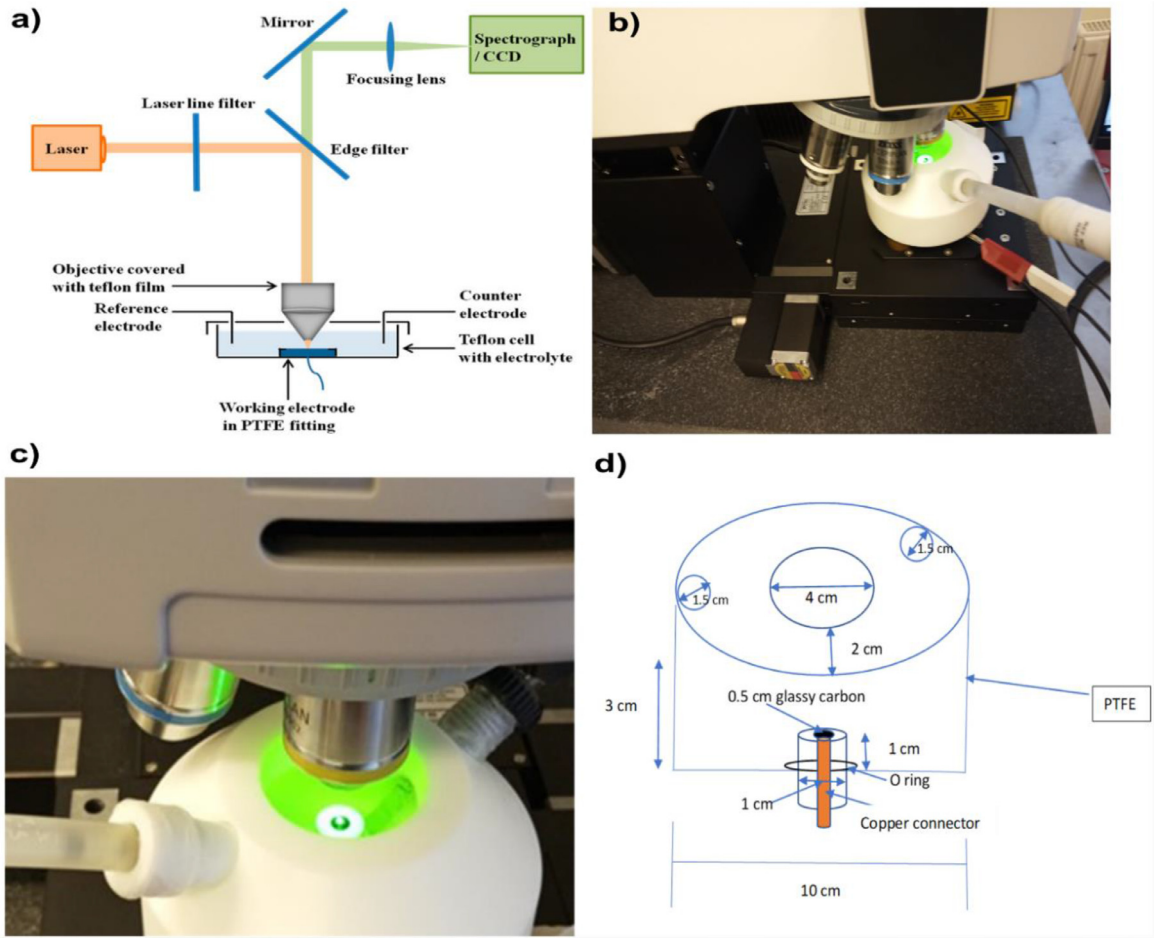

Fig. 1. a) Schematics of the concept of in-situ electrochemical Raman spectroscopy reproduced with permission from American Chemical Society (ACS) [27], b), c) actual images, and d) cell design of the in-situ Raman electrochemical cell used in this work [28].

resistance, which was measured by the EIS technique. The potential was compensated by the following equation:

$$E_{\text{compensated}} = E_{\text{measured}} - iR \tag{1}$$

where $E_{\text{compensated}}$ and E_{measured} are compensated and measured potentials, respectively.

The Hg/HgO potentials were converted to RHE by measuring the voltage at zero current of the HER curve in a hydrogen-saturated electrolyte on Pt electrodes. The Hg/HgO reference electrode potential was converted to RHE in 1 M KOH using the following equation:

$$E_{\text{vsRHE}} = E_{\text{vsHg/HgO}} + 0.9 \tag{2}$$

All the reported current densities were normalized to the geometric area of the electrode.

The electrochemical active surface area (ECSA) was measured by the electrochemical double-layer capacitance method. Then capacitance from 0.9 to 1 V vs RHE at scan rates of 50, 100, 150, 200, 250 mV/s. The CV used for electrochemical double-layer capacitance (C_{dl}) calculation was acquired in a potential window where no Faradaic process occurred. To derive the C_{dl}, the following equation was used:

$$C_{dl} = \frac{I_c}{\nu} \tag{3}$$

where C_{dl} is the double-layer capacitance (mF/cm^2) of the electroactive materials, I_c is the charging current (mA/cm^2), and ν is the scan rate (mV/s).

Chronoamperometry was measured at a fixed potential (−0.4 V vs. RHE) for 30 h. The stability of the catalyst material was also evaluated using an accelerated stress test (AST). AST was carried out by cycling the electrode between −0.8 to −1.3 V at a scan rate of 100 mA/cm^2 for 5000 cycles. The Hg/HgO reference electrode was calibrated versus a reversible hydrogen electrode (RHE) in 1 and 0.1 M KOH. The electrochemical data shown are average data from 3 inks from every powder for each catalyst.

2.3. In situ Raman measurements

In situ Raman measurements were carried out with a lab-made Teflon cell. The catalyst deposited on GC (pine research), a carbon paper (fuel cell store), and Hg/HgO (Pine Research) was used as a working, counter, and reference electrode, respectively as in Fig. 1. In situ Raman spectra were collected using a WITec alpha300 R Confocal Raman microscope [532 nm laser with a power of 5.0 mW] coupled with Zeiss EC Epiplan 10x objective and G1: 600 g/mm BLZ=500 nm grating. The GC surface was polished with μm-sized alumina powders, then sonicated in 1 M KOH for 5 min and then rinsed with water and dried in air. The experiments was carried out using purified N_2-saturated 1 M KOH electrolytes. The laser is emitted on the working electrode through a transparent quartz glass window that reduces contamination and interference. All the experiments were conducted at room temperature (20 ± 2 °C). All the data points were processed using origin software.

In situ Raman-chronoamperometry study was done at −0.4 V vs. RHE for 30,000 s for NiCu catalysts. The Raman spectra were

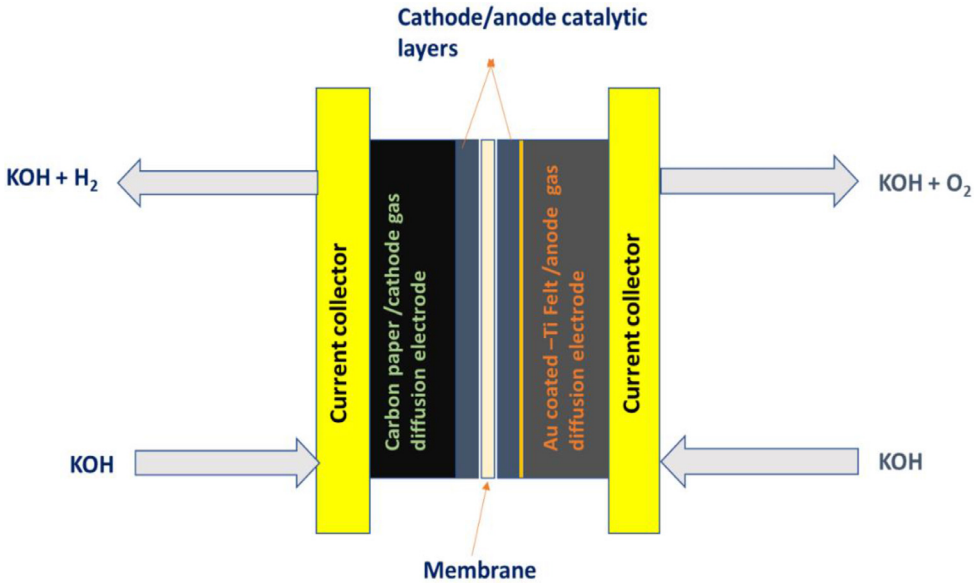

Fig. 2. Schematic of the membrane electrode assembly for AEM water electrolyzer.

collected at the applied potential in 1 M KOH every 10 sweeps (10 s/sweep) from 100 to 2000 cm^{-1}. The spectrum shift of silicon wafer Raman peak at 520.7 cm^{-1} was used for calibration.

2.4. Membrane electrode assembly (MEA) fabrication and pretreatment

Catalyst inks were fabricated by mixing catalyst powder with water: isopropanol (1:1), and ionomer (Fumion FAA-3-SOLUT-10 (Fuel Cell Store)). The solution was sonicated for 30 min to ensure fine and well-dispersed ink. Cathode catalysts loadings were 1 mg/cm^2 for Pt/C (60 wt% metal on support, Alfa Aesar) and 5 mg/cm^2 for 60 wt% NiCu MMO/Ketjen black. An Ir black benchmark catalyst with a loading of 3 mg/cm^2 (Alfa Aesar) was used at the anode for all MEAs. Catalyst layers were sprayed at 60 °C using a Coltech airbrush (0.35 mm nozzle) on Toray 090 carbon paper (25 cm^2, Fuel Cell Store) for the cathode, and Ti felt (Bekaert Inc.) coated with Au for anode as catalyst coated substrates (CCSs). The area of carbon paper equals the area of Ti felt and represents the electrode surface area (25 cm^2). The Ti felt was pretreated by etching in HCl (37 wt%, Sigma Aldrich) for 2 min to remove the non conductive surface oxide and then sonicated for 5 min in water and ethanol before being sputter-coated with Au using an Edwards sputter coater to reduce interfacial contact resistance (ICR) within the cell. The coating was carried out at a vapor deposition pressure of 0.15 atm at 20 mA for 2 min on each side. The ionomer content amounted to 25 and 7 wt% of the total solids in ink for cathode and anode, respectively. The membrane, Fumapem-3-PE-30, was sandwiched between cathode and anode gas diffusion electrodes as in Fig. 2. The MEAs were conditioned and exchanged to the OH form in 1 M KOH overnight. The AEM water electrolyzer setup consisted of a 5 L Teflon tank with heaters and a peristaltic pump. Tests were conducted at $T = 50$ °C. The concentrations of KOH employed were 1 and 0.1 M KOH (ACS reagent, ≥85%, pellets, Sigma Aldrich). The flow rates of the pumps were 250 ml/min.

2.5. Polarization curve and electrochemical impedance measurements

A high-current potentiostat (HCP-803, Biologic) was used to control cell voltage and measure impedance in the single-cell measurements. The polarization curve was recorded galvanostatically, ramping the current from 0 to 2 A/cm^2 at a rate of 80 mA/cm^2 per minute. Electrochemical impedance spectroscopy (EIS) was employed to determine the cell resistances and performed at different current densities, such as 0.2 A/cm^2, in the AC frequency range of 100 kHz–1 Hz. The NiCu MMO catalytic layers were post analyzed by SEM and EDX.

3. Results and discussions

3.1. Structural characterization

SEM and STEM images of the nickel-copper catalyst synthesized by chemical reduction with the addition of Na_2CO_3 and annealed in 5% H_2/Ar (NiCu MMO) are shown in Fig. 3. The Figs. 3a and 3b show that NiCu MMO catalysts have dense areas of agglomerated nanosheet morphology. The STEM image in Fig. 3c displays that NiCu MMO nanosheets are loaded on the carbon support (Ketjen black EC-600JD) with a dark thick region of NiCu nanosheets. Fig. 3d confirmed the loosely stacked nanosheets morphology of NiCu MMO catalysts. Similar catalyst morphology produced by chemical reduction by sodium borohydride has given various names from nanocotton [29], nanosponges [30–32, and nanosheets [33–39] and in this work, we will refer to these catalysts as nanosheets. During the chemical reduction process, sodium borohydride reacts quickly with transition metal cations to precipitate metal boride M_xB_y species [39–42]. In the case of NiCu MMO, Na_2CO_3 was added during the synthesis process to precipitate oxide species [21]. We investigated another nickel-copper catalyst without the addition of Na_2CO_3 and annealed the resulted powder in the air (NiCu oxide) and 5% H_2/Ar (NiCu alloy) and they exhibited also an agglomerated nanosheets morphology similar to NiCu MMO as seen in (Fig. S1). Energy dispersive x-ray spectroscopy (EDX) of NiCu MMO is shown in Fig. 4a. The EDX spectrum displays peaks corresponding to Ni, Cu, O, and C with Ni: Cu weight percentage as 52.3:47.7, which is in good agreement with precursors percentage. The EDX spectrum displays peaks corresponding to Ni, Cu, O, and C. Impurities or remaining elements from the synthesis process appear to be absent.

The XRD pattern of NiCu MMO in Fig. 4b shows peaks at 2θ values of 32.5°, 35.6°, 37.2°, 38.9°, 43.2°, 44.56°, 48.9°, 51.93°, and 62.8°. The diffraction peaks at 2θ values of 44.5° and 51.93° are

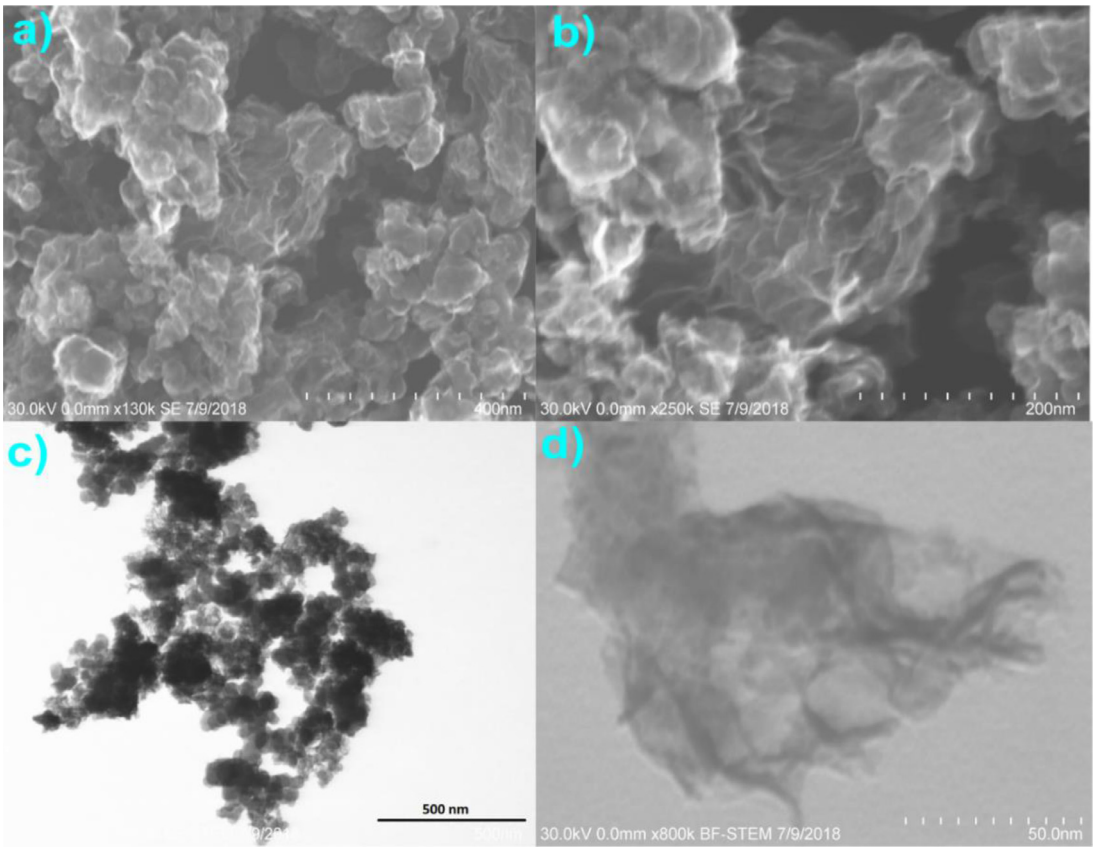

Fig. 3. a) and b. SEM images, c) STEM image NiCu MMO supported on Ketjen black, and d) high magnification STEM image of NiCu MMO nanosheets.

associated with Ni (111) and Ni(200) crystal planes of nickel face-centered cubic (FCC) structure with (JCPDS card No. #04–0850) [43]. The peaks at 2θ values at 37.2°, 43.2°, and 62.8° correspond to (111), (200), and (220) diffraction planes of NiO (JCPDS card no. #47–1049) [44]. The diffraction peaks at 2θ values of 32.5°, 35.6°, 38.9°, 48.9° values correspond to CuO crystal structure (JCPDS card no. #80–0076) [45].

NiCu alloy shows peaks at 2θ values of 44.5° and 51.93° that correspond to pure Ni (JCPDS No. 04–0850) [43] while the peaks at 44° and 51.2° correspond to pure Cu (JCPDS No. 04–0836) [46]. While NiCu oxide shows peaks at 2θ values of 37.2°, 43.2°, and 62.8° correspond to NiO (JCPDS card no. #47–1049) and peaks at 2θ values of 32.5°, 35.6°, 38.9°, 48.9° of CuO crystal structure (JCPDS card No. #80–0076) [44,45]. The NiCu MMO vibrational modes were characterized by Raman spectroscopy in Fig. 4c. The Raman spectrum in Fig. 4c shows Raman peaks at 490, 606, 810, 1020, and 1100 cm^{-1} respectively. The Raman peak at 490 cm^{-1} corresponds to $Cu(OH)_2$ while the Raman peak 606 cm^{-1} corresponds to the B_g Raman mode of CuO [47–50. The Raman peaks at 810, 1020, and 1100 cm^{-1} correspond to two-phonon (2P) NiO vibrational modes [51–55.

XPS analysis provides sensitive information about the surface chemical composition of NiCu MMO catalyst. NiCu MMO survey spectrum is shown in Fig. 4d. The survey spectrum indicates the presence of Ni, Cu, B, O, and C peaks. Ni 2p high-resolution XPS spectrum is shown in Fig. 5a and 5b. The Ni 2p XPS spectrum is divided into two main peaks (Ni-$2p_{1/2}$ and Ni-$2p_{3/2}$) due to the spin-orbit effect and two oxidation states for nickel (Ni^0 and Ni^{2+}) can be deconvoluted. The XPS peaks at 853.8 eV and 871.4 eV can be assigned to Ni $2p_{3/2}$ and Ni $2p_{1/2}$ of Ni^0 [20,56]. The XPS peaks located at 855.4 eV with a satellite at 860.9 eV correspond to Ni $2p_{3/2}$ of Ni^{2+}. The peak at 872.5 eV with a satellite at 879.4 eV can be attributed to Ni $2p_{1/2}$ of Ni^{2+} [20,56] Cu-2p high-resolution spectrum is shown in Fig. 5c and 5d. The XPS peaks at 932.6 eV and 952.4 eV correspond to Cu $2p_{3/2}$ and Cu $2p_{1/2}$ of Cu^0 [57]. The XPS peak at 933.7 eV corresponds to CuO [58]. The peaks at 934.8 and 954.4 eV are associated with $Cu(OH)_2$ [58]. $Cu(OH)_2$ appears to form due to CuO reaction with chemisorbed water on the catalyst surface.

The high-resolution Ni 2p XPS spectrum in NiCu alloy exhibits peaks at 852.4 and 869.5 eV which correspond to Ni $2p_{3/2}$ and Ni $2p_{1/2}$ peaks of metallic Ni^o) Fig. S2a ([59]. The Cu 2p spectrum shows two peaks at 932.5 and 952.3 eV which are assigned to Cu $2p_{3/2}$ and Cu $2p_{1/2}$ of metallic Cu^0 (Fig. S2b) [16].

The high-resolution XPS spectrum of Ni 2p in NiCu oxide shows that the Ni $2p_{3/2}$ main peak and its satellite at 854 and 862 eV, and the Ni $2p_{1/2}$ main peak and its satellite at 872 and 879 eV, respectively confirming the presence of Ni^{+2} state (Fig. S2c) [60]. The high-resolution XPS spectrum of the Cu 2p spectrum of NiCu oxide shows peaks at 933.7, 943.1, 954.3, 962.9 eV. The peaks at 933.7 and 954.3 eV correspond to the Cu $2p_{3/2}$ and Cu $2p_{1/2}$, respectively. Also, there are two satellite peaks centered at about 943.1 and 962.9 eV, demonstrating the presence of Cu^{+2} state (Fig. S2d) [61].

Based on the structural characterization. NiCu mixed metal oxide (MMO) nanosheets have Ni, NiO, CuO phases and hydroxide species such as $Cu(OH)_2$ which can be beneficial for HER in alkaline electrolytes [62] as we will see from the electrochemical measurements. NiCu alloy contains pure Ni and pure Cu phases while NiCu oxide contains NiO and CuO phases.

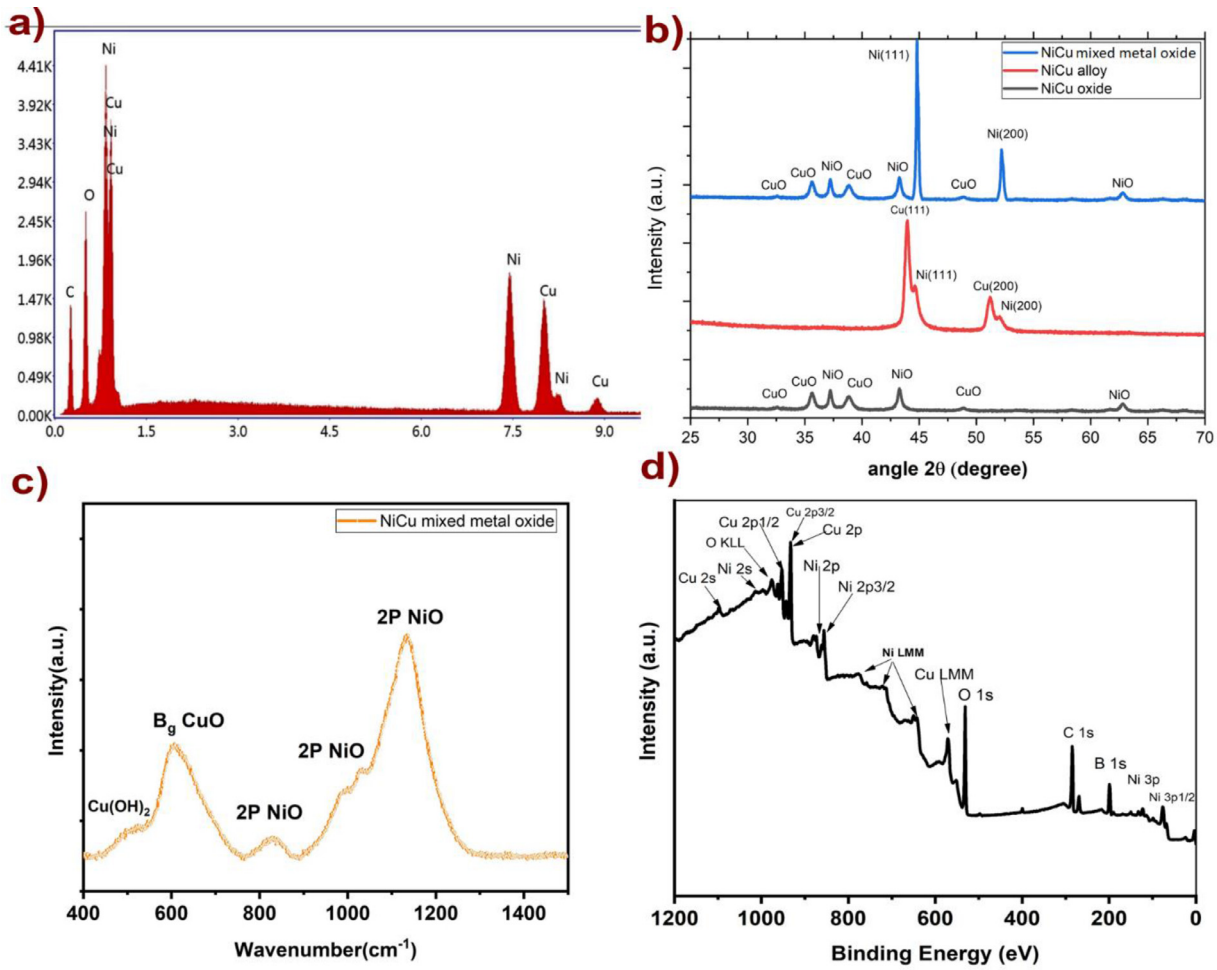

Fig. 4. a) EDX spectrum of NiCu MMO catalyst, b) XRD spectrums of NiCu alloy, NiCu MMO, and NiCu oxide catalysts, c) Raman spectrum and, d) XPS survey spectrum of NiCu MMO catalyst.

3.2. Electrochemical characterization

Fig. 6a shows linear sweep voltammetry (LSV) curves of NiCu alloy, NiCu MMO, and NiCu oxide in 1 and 0.1 M KOH. All catalyst loadings were equal to 250 μg/cm^2. NiCu MMO has the highest HER activity in 1 M KOH by achieving −10 mA/cm^2 at −200 mV compared to the −250 and −300 mV for NiCu alloy and NiCu oxide, respectively, to obtain the same current density. As seen from Fig. 6a, the current density normalized to geometric surface area for NiCu MMO at −0.35 V vs RHE in 1 M KOH is five times higher than 0.1 M KOH. However, the activity trend for the nickel-copper catalysts is the same in 0.1 M KOH. Fig. 6b shows a comparison between the NiCu MMO HER activity and data from the literature. The NiCu MMO shows one of the best mass active HER catalytic activities reported in Table S1, Table S2, and Fig. 6b.

The LSV curves in Fig. 6a show that the HER activity increases with increasing KOH electrolyte concentration, which in agreement with literature [63,64]. Lasia et al. found that the rate constants of Volmer and Heyrovsky reactions depend on the bulk OH^-concentrations [65]. An appropriate rise of the KOH electrolyte concentration increases hydroxide ion activity [64–67]. Recently Wang et al. showed that the high HER activity at high KOH concentration is due to H_3O^+ intermediates generated on nanocatalyst surface [68].

Electrocatalytic active surface area (ECSA) measurements were carried out to evaluate the intrinsic catalytic activity of nickel-copper catalysts. The ECSA was estimated by measuring the electrochemical double-layer capacitance (C_{dl}) from cyclic voltammograms at various scan rates over a non-faradaic (totally polarized) potential range, as in Fig. S3 in the Supplementary Information. The NiCu MMO catalysts exhibit the largest double-layer capacitance C_{dl} of 9.16 (mF/cm^2) compared to those of the NiCu alloy (6.58 mF/cm^2) and the NiCu oxide (3.80 mF/cm^2), showing that a larger ECSA of NiCu MMO allows more exposed active sites to promote HER performance. The specific surface area of the NiCu catalysts was also investigated with Brunauer–Emmett–Teller (BET) measurement (Figure S3, ESI†). The specific surface area has a similar trend as ECSA. NiCu MMO possesses a surface area of 156 m^2/g which is far higher than that of NiCu alloy (112 m^2/g) and NiCu oxide (92 m^2/g). When normalized to electrochemical surface area (Fig. S3, ESI†) the differences in catalyst activity become less, especially in the lower potential range. However, NiCu MMO still possesses the highest intrinsic activity.

The linear regions of Tafel plots in Fig. 6c are fitted to the Tafel equation, yielding Tafel slopes of 120, 130, and 195 mV/dec for NiCu MMO, NiCu alloy, and NiCu oxide respectively. The kinetic parameters for the nickel-copper catalysts (j_o and b) presented in Table 1 were derived from the Tafel equation:

$$\eta = a + b \log j \tag{4}$$

Where η (V) is the applied overpotential, j (mA/cm^2) is the current density, b (V/dec) is the Tafel slope, and a (V) is the intercept.

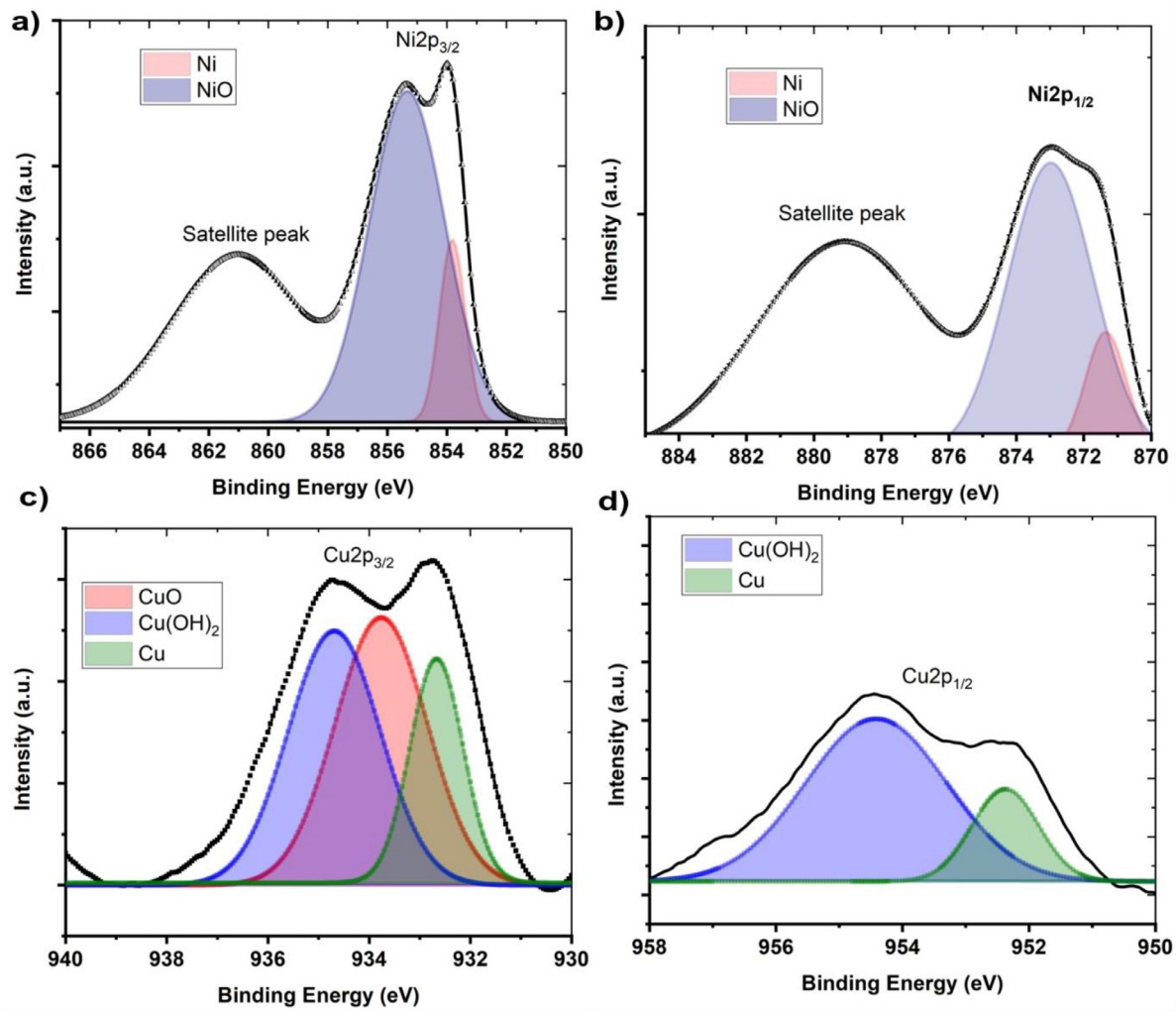

Fig. 5. High-resolution XPS spectrum of a) Ni $2P_{3/2}$, b) Ni $2p_{1/2,}$ c) Cu $2p_{3/2,}$ d) Cu $2p_{1/2}$ of NiCu MMO catalyst.

Table 1
Overpotential at −10 mA/cm^2, Tafel slope b, charge transfer resistance (α), and exchange current density j_0 for NiCu catalysts in 1 M KOH.

Catalyst	Overpotential (V) at −10 mA/cm^2	Tafel Slope mV/decade	charge transfer coefficient(α)	J_o (μA/cm^2)
NiCu alloy	−0.250	130±2	0.454	9.70
NiCu oxide	−0.300	195±1	0.302	4.62
NiCu MMO	−0.200	120±2	0.492	9.98

The exchange of current density j_o can be obtained by extrapolating the Tafel plots to the x-axis or assuming η is zero.

$$a = (2.3RT)/(\alpha F)\log j_o$$
$$b = (2.3RT)/(\alpha F) \quad (5)$$

where R is the gas constant (8.314 kJ mol^{-1} K^{-1}), T is the temperature in K, α is the charge-transfer coefficient, and F is the Faraday constant (96,485 C mol^{-1}).

Table 1 summarizes the kinetic parameters for nickel-copper catalysts. NiCu MMO shows the lowest Tafel slope and highest charge transfer coefficient and exchange current density over NiCu alloy and NiCu oxide which confirms the superior activity of NiCu MMO.

In view of the Tafel slope being close to 120 mV/dec, it is likely that the charge transfer coefficient represents the symmetry factor of the Volmer step in this case. The Tafel slopes reflect an intensive property of the HER catalysts from which some indication about the reaction mechanism of the HER and the rate-determining step (*rds*) can be obtained. The Volmer reaction involves the electroreduction of water molecules with hydrogen adsorption as in Eq. (6), while the Heyrovsky's reaction involves electrochemical hydrogen desorption eq (7). The Tafel reaction involves chemical desorption Eq. (8) [65].

$$M + H_2O + e^- \leftrightarrow MH_{ads} + OH^- \quad \text{Volmer} \quad (6)$$

$$MH_{ads} + H_2O + e^- \leftrightarrow H_2 + M + OH^- \quad \text{Heyrovsky} \quad (7)$$

$$MH_{ads} + MH_{ads} \leftrightarrow H_2 + M \quad \text{Tafel} \quad (8)$$

A detailed analysis shows that *rds* for the HER at NiCu MMO is the Volmer reaction, then a Tafel slope in the order of 120 mV would result. Whether the next step in the reaction sequence is the Heyrovsky or Tafel step [65] cannot be determined by this analysis, however.

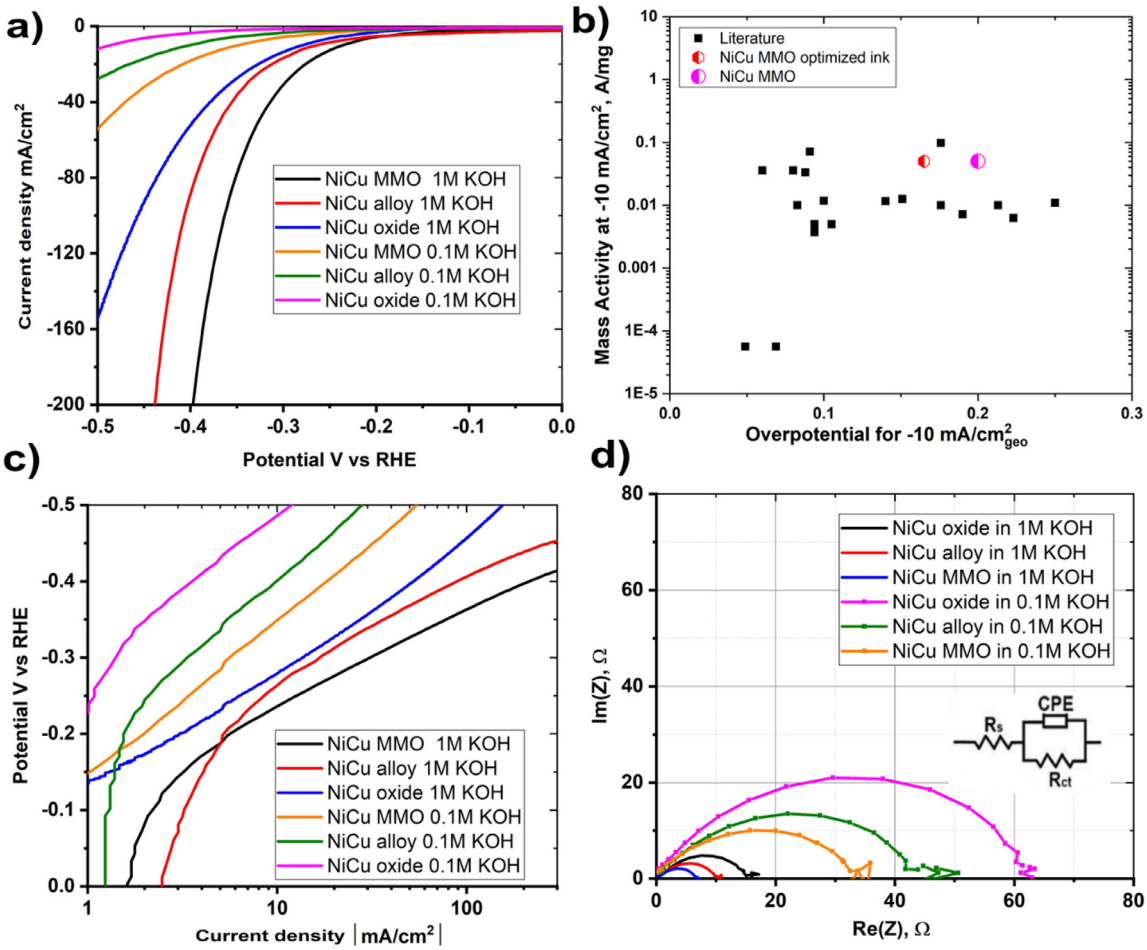

Fig. 6. a) HER LSV curves NiCu alloy, NiCu MMO, and NiCu oxide in 0.1 and 1 M KOH using Nafion ionomer (ionomer to catalyst weight ratio = 0.2), b) Comparison of mass activity and overpotential to achieve to −10 mA/cm^2 for hydrogen evolution catalysts, data reproduced from Kibsgaard et al. [69] and Table S2 (supplementary information) c) Corresponding Tafel slopes of NiCu alloy, NiCu MMO, and NiCu oxide, d) Impedance complex plane plots of NiCu alloy, NiCu MMO, and NiCu oxide at −250 mV.

Fig. 6d shows impedance complex plane plots of NiCu alloy, NiCu oxide, and NiCu MMO in 0.1 and 1 M KOH at an applied potential of −250 mV vs. RHE after subtracting ohmic resistance. In the complex plane plots, only one semicircle is observed, which can be attributed to a charge transfer process related to the HER [70–72]. The charge transfer resistance (R_{ct}) is represented by the diameter of the semicircle. The radius of the semicircle decreases at higher KOH concentration, signifying a lower charge transfer resistance (R_{ct}) and a higher rate of hydrogen evolution. NiCu MMO exhibit R_{ct} value of 6.96 Ω at an applied potential of −250 mV compared to NiCu alloy (10.38 Ω) and oxide (13.81 Ω) which further confirm the superior activity, faster reaction kinetic and high electron transfer efficiency of NiCu MMO [72].

The equivalent circuit for the NiCu alloy, NiCu MMO, and NiCu oxide in Fig. 6d is characterized by a single time constant, and we modeled the impedance by a series resistance (R_s, related to ohmic solution resistance), in series with one parallel circuit consisting of a charge transfer resistance (R_{ct}) and a constant phase element (CPE) related to the double-layer capacitance. This equivalent circuit has previously been used in literature to describe HER on polycrystalline Ni and Ni-based materials [73]. (The constant phase element (CPE) was used instead of capacitance due to frequency dispersion and the appearance of depressed semicircles in the impedance plane plots). The charge transfer resistance (R_{ct}) represents the kinetics of the HER at the electrode/electrolyte interface. The absence of Warburg impedance indicates that mass transport is rapid enough so that the reaction is kinetically controlled [70,71,74]. The impedance complex plane plots for different applied overpotentials are shown in Fig. S4a in the ESI†, and these show that the R_{ct} decreases with increasing potential as it would if the current-voltage relationship is described by Eq. (4) above. (The lower R_{ct} value at higher potential reflects the exponential dependence of the current on the overpotential and thus the accelerated electron transfer and higher rates of the HER at higher overpotential [70,71,74]. As can be shown by a simple differentiation of Eqn. 4 above, the Tafel slope may be obtained from plots of potential vs. log $(R_{ct})^{-1}$. From our plots, we obtain 120 mV/dec, see Supplementary Information, Figure S4b, which is the same as that obtained from the LSV curves. The same Tafel slope being obtained with impedance spectroscopy thus validates the iR-corrected linear-sweep voltammograms.

Fig. 7a shows the current vs. time recorded in chronoamperometric measurements performed by applying a constant potential of −400 mV for 30 h on NiCu alloy, NiCu MMO, and NiCu oxide. For all samples but NiCu MMO in 0.1 M KOH, the current density decreases (i.e. the activity decreases) rapidly during the first few minutes. For NiCu MMO in 0.1 M KOH and NiCu oxide in 1 M KOH, the current density then levels off and remains constant at approximately −11 mA/cm^2 and −50 mA/cm^2, respectively. NiCu oxide shows stable performance at −50 mA/cm^2 for 30 h. For NiCu alloy in 1 M KOH, the current density slowly increases (activity increases) with time from approximately −90 mA/cm^2 to −100 mA/cm^2 after 30 h. For the NiCu MMO sample in 1 M KOH, the current density reaches a minimum activity after

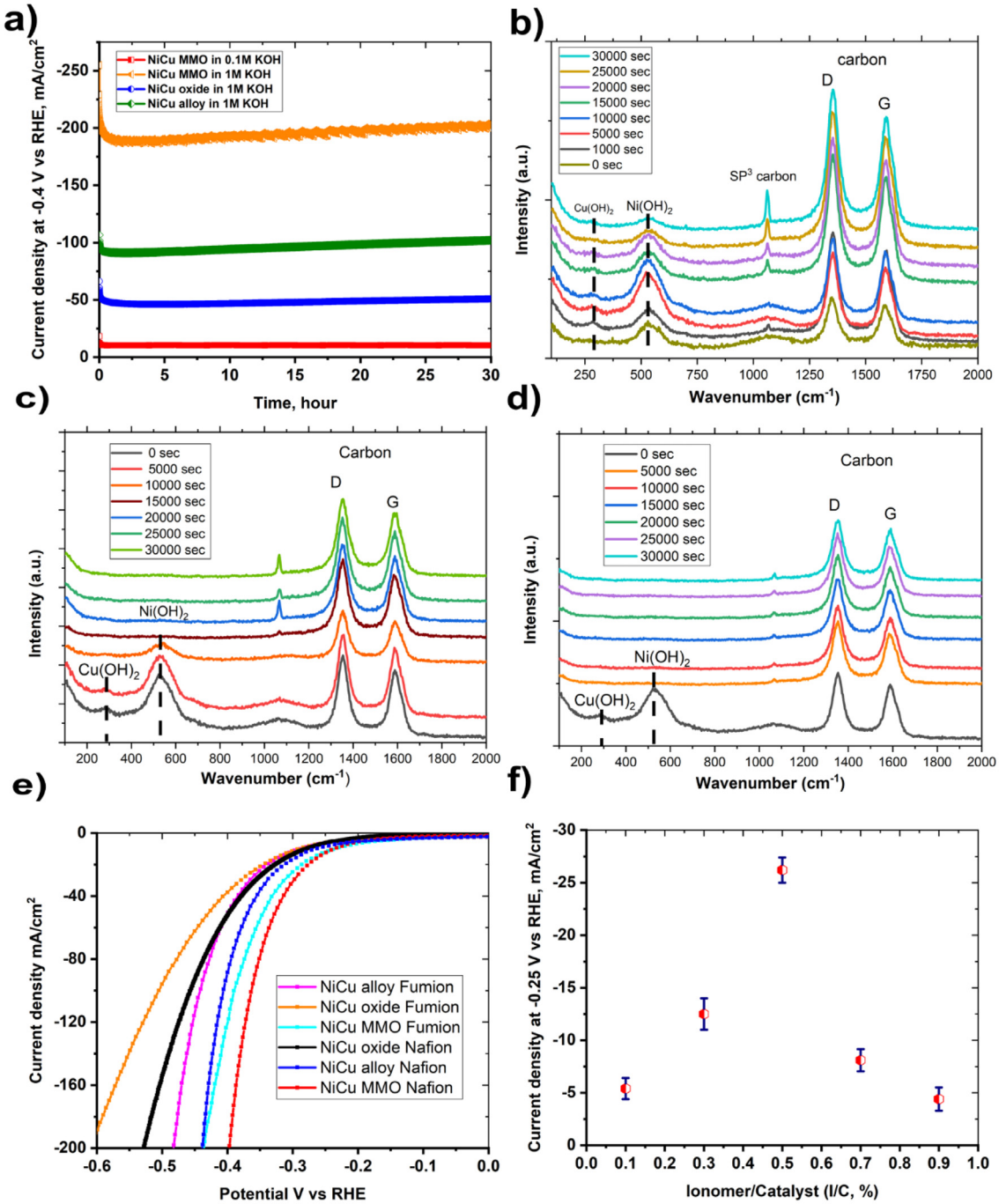

Fig. 7. a) Chronoamperometry measurement of NiCu alloy, NiCu MMO, and NiCu oxide using Nafion ionomer in KOH electrolytes, b) In situ Raman spectra of NiCu MMO under chronoamperometric HER conditions (−0.4 V vs RHE) at different time intervals in 1 M KOH, In situ Raman spectra of c) NiCu oxide and d) NiCu alloy under HER conditions (−0.4 V vs RHE) at different time intervals, e) HER LSV curves of NiCu alloy, NiCu MMO, and NiCu oxide using Nafion and Fumion ionomers in 1 M KOH, f) Current density at −0.25 V at different ionomer to catalyst weight ratios (I/C) of NiCu MMO.

approximately 30 min at which the current density is approximately −180 mA/cm^2, and then slowly increases to a little below −200 mA/cm^2 at 30 h. The chronoamperometric measurements confirm the higher HER activity of NiCu MMO in 1 M KOH than in 0.1 M KOH and over NiCu alloy and NiCu oxide in the same electrolyte. The current densities observed from chronoamperometry are in good agreement with those observed in the LSVs.

Fig. 7b shows in-situ Raman spectra of NiCu MMO under an applied potential of −0.4 V vs RHE at different time intervals. All the spectra in Fig. 7b display peaks at 292, 530, 1060, 1350, and 1585 cm^{-1}. The peak at 292 cm^{-1} can be assigned to copper hydroxide $Cu(OH)_2$ species [47] while the peak at 530 cm^{-1} can be assigned to nickel hydroxide $Ni(OH)_2$ [75]. The peak at 1060 cm^{-1} can be assigned to carbonates [76] while the peaks at 1346, and 1585 cm^{-1} correspond D band, and G band peaks of carbon respectively [77,78]. The spectra show clear peaks of $Ni(OH)_2$ and $Cu(OH)_2$ at the beginning of HER. However, the $Cu(OH)_2$ peaks decreased more significantly than the $Ni(OH)_2$ peaks. In other words, whereas both $Cu(OH)_2$ and $Ni(OH)_2$ both exist during the entire period of 30,000 s, both Cu and Ni hydroxides get slowly reduced,

but Cu more so than Ni. The reduction of these elements is consistent with the Pourbaix diagrams of Cu and Ni which predict that both $Ni(OH)_2$ and $Cu(OH)_2$ would be reduced to metallic nickel and copper at this potential [79].

The NiCu oxide also displayed peaks corresponding to $Ni(OH)_2$ and $Cu(OH)_2$, but these peaks disappeared completely after 15,000 s, as shown in Fig. 7c. However, the HER activity of the NiCu oxide is much lower than that of NiCu MMO. This confirms the importance of the presence of metallic species on the catalyst surface, as found by Danilovic et al. [80], for superior HER activity.

Finally, the Raman spectrum for the NiCu alloy catalyst also shows peaks related to $Ni(OH)_2$ and $Cu(OH)_2$ surface species when the catalyst is immersed in KOH, which confirmed the hypothesis that Ni metal will convert to oxide species once in contact with KOH [80,81]. The hydroxide species on the NiCu alloy gets reduced rather rapidly (< 5000 s) at the surface, as shown in Fig. 7d, compared to NiCu MMO and NiCu oxide and did not lead to exceptional activity compared to NiCu MMO.

NiCu MMO thus showed the best HER activity in the alkaline electrolytes with a Tafel slope of 120 mV/dec. The bifunctional system of NiCu MMO catalyst includes Ni metal, NiO, and CuO oxides, and provide a rapid Volmer step and thus rapid overall HER reaction kinetics. The improved HER kinetics of the NiCu MMO can be attributed to the presence of both Ni and NiO where NiO sites to facilitate water dissociation and bind OH_{ad} while Ni metallic binds H_{ads} and CuO stabilizes NiO under HER conditions. Similarly, Bates et al. found that the synergistic HER enhancement of Ni/NiO is due to NiO content and Cr_2O_3 appears to stabilize NiO under HER conditions [82]. The in situ Raman results show that the presence of both metal and oxide phases is essential to sustain a high HER activity, the performance of NiCu MMO relative to that of NiCu alloy or NiCu oxide. We relate this to the in situ Raman data showing that copper hydroxide gets reduced and nickel hydroxide is to some extent preserved under HER conditions.

We attribute the rapid decay in electrocatalytic activity in all samples to an initial and rapid adjustment of the surface state of all catalysts, whereas the long-term behavior is more complex. For the NiCu oxide, there is no further change in the surface state after 15000s (Fig. 7c), and the electrocatalytic activity remains the same as that immediately after the initial transient. The current transient is thus fully consistent with the Raman spectra for NiCu oxide in Fig. 7c. Since the Raman spectra of the NiCu alloy (Fig. 7d) indicate a surface at which hydroxides are completely absent after 5000 s, however, the slow increase in catalytic activity with time in Fig. 7a for this catalyst may be related to a slow change in the composition or surface area, i.e. to catalyst instability. For NiCu MMO in 1 M KOH, the initial transient is followed by a slower increase in catalytic activity. A correspondingly slow change in the surface state, c.f. the Raman spectra in Fig. 7b, appear to persist throughout the chronoamperometry experiment.

We relate this difference to the synthesis. For the NiCu alloy, only a thin layer of the hydroxides will form as the NiCu alloy is exposed to the KOH solution. This layer is rapidly reduced as the catalyst is subjected to a negative potential. However, since there is no indication of any metal phase in the NiCu oxide in the diffractograms, we may assume that during exposure to negative potentials these catalysts will be reduced continuously until the entire catalyst is converted to metal. For the NiCu MMO, this seems to have combined behavior (mixed metal oxide (Ni-NiO-CuO) catalyst), since the oxidation due to the annealing is not complete, c.f. the diffractograms in Fig. 4b which displays a substantial peak corresponding to Ni(111). This catalyst heterogeneity of metallic and oxide phases will cause mixed behavior of a continuous but slow change in the surface state throughout the experiments, which may be related to a slow diffusion-limited process in the sample. The surface is therefore also slowly reorganized and will consist of a mix of phases and a slowly changing activity.

NiCu MMO also showed good stability during an accelerated stress test consisting of 5000 potential cycles from between −0.8 to −1.3 V at a scan rate of 100 mV/s. The LSV for NiCu MMO before and after the procedure showed only a 20 mV difference in the potential required to achieve - 100 mA/cm^2 as shown in Fig. S5 ESI†.

Fig. 7e shows The HER activity using Nafion and anion exchange ionomer (Fumion ionomer) of NiCu alloy, NiCu MMO, and NiCu oxide. The activity for the HER of nickel-copper catalysts decreased if Fumion ionomer replaced Nafion in the catalyst ink, and resulted in a potential shift of 30 mV at −100 mA/cm^2 as compared to the Nafion ionomer. Catalyst inks with Nafion resulted in higher HER activity compared to catalyst inks with Fumion ionomer. We assign the difference in activity between catalysts in inks with Nafion and those with Fumion ionomers to the nature of the ionomer backbone and its chemistry (ammonium-, imidazolium-, phosphonium-based compounds in anion exchange ionomers such as Fumion, or sulphonic acid groups (SO_3^-) in Nafion) [83,84]. The SO_3^- moiety in Nafion interacts only weakly with the catalyst surface, and the effect of SO_3^- adsorption on electrocatalyst performance is expected to be negligible, particularly in the HER region where the negative charge on the catalyst surface would repel sulfonate species [21]. The quaternary ammonium (QA) functional group used for OH^- transport in anion exchange ionomer (AEI), on the other hand, appears to poison NiCu MMO catalyst and block active catalyst sites. Fumion ionomer shows higher total polarization resistance than Nafion as shown in the impedance complex plane plot of NiCu MMO using Nafion and Fumion ionomers (Fig. S6.a). The small semicircle at the low-frequency region for Fumion ionomer (Fig. S6.a) has been suggested to correspond to quaternary ammonium adsorption [85]. The results show that the anion ionomer not only serves as a binder but also affects the electrocatalyst's HER activity [4].

We consequently investigated the impact of the Nafion ionomer content to find the composition at which the HER performance peaks for NiCu MMO. The results are shown in Fig. 7f. The HER activity thus increases with increasing Nafion ionomer to the catalyst weight ratio (I/C), and a maximum appears at a weight ratio of I:C of 0.5. The NiCu MMO at I/C = 0.5 achieves −10 mA/cm^2 at 170 mV, which indicates better catalyst utilization, lower total polarization resistance, and optimum HER performance as shown in Fig. S6b and S6c. The low performance with a low ionomer content is attributed to the poor dispersion of the ink. At high ionomer content, the HER activity is small due to increased aggregation of Nafion and the associated blocking of mass transport and active sites [25]. The moderate I/C ratio indicates that Nafion improves the catalyst dispersion and distribution and reduced transfer resistance. The optimized ionomer content provides an efficient pathway for OH^- (in the aqueous electrolyte) and electrons and forms a stable reaction interface [86].

3.3. Anion exchange membrane (AEM) electrolysis

To test the activity of NiCu MMO in an actual AEM electrolysis environment, NiCu MMO and Ir black MEAs were fabricated and mounted in an AEM water electrolysis cell as explained in the Supplementary Information and Fig. S7 ESI†. Two types of MEAs will be mentioned in Results Pt/C cell and NiCu MMO cell for NiCu MMO-Ir and Pt/C-Ir cells respectively. Fig. 8 shows the impedance complex-plane plot at 0.2 A/cm^2 for NiCu MMO cells (Fig. 8a) and Pt/C cells (Fig. 8b) in 0.1 and 1 M KOH. The impedance complex-plane plots appear to consist of two partly overlapping

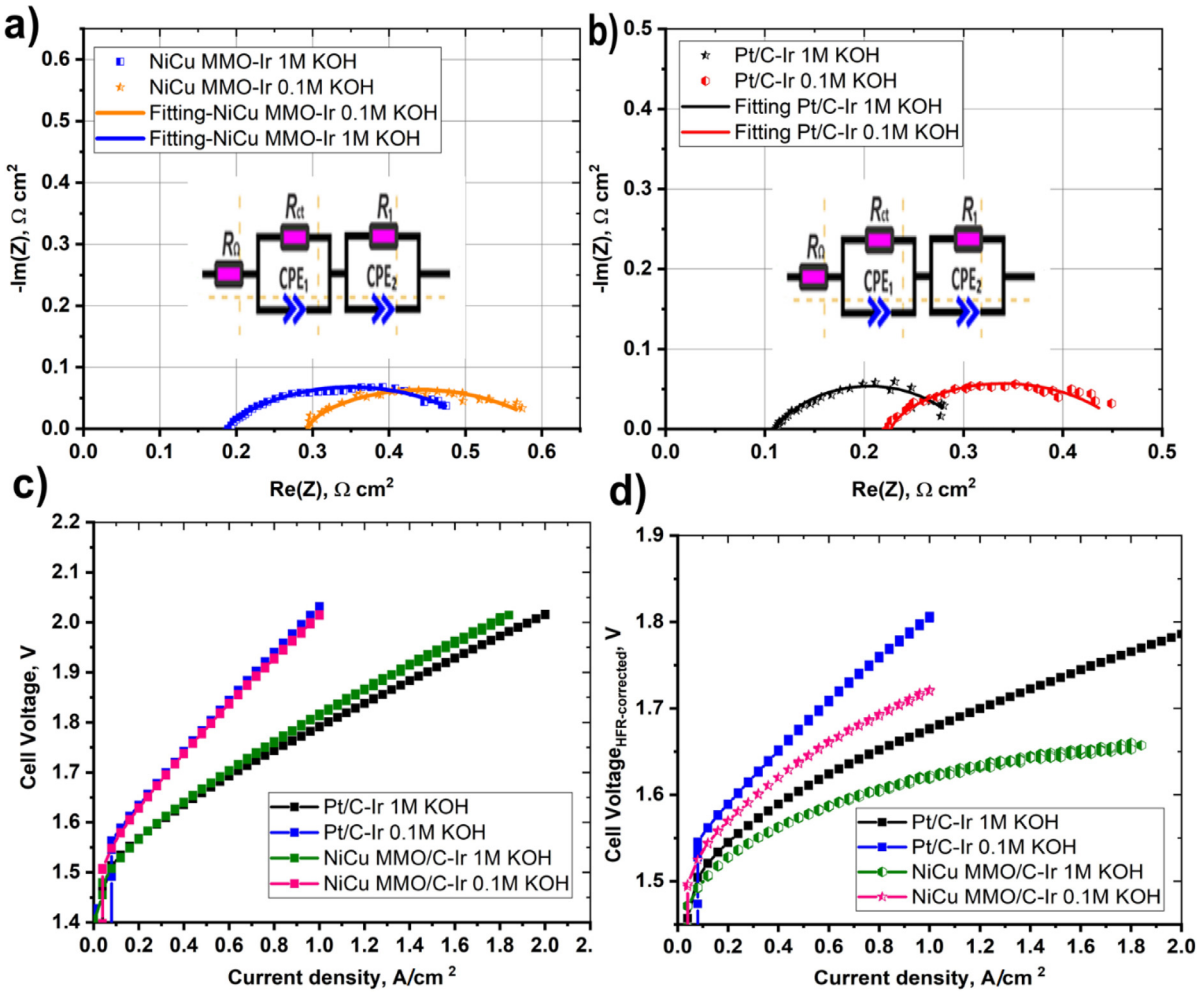

Fig. 8. a) Impedance complex plane plot of NiCu MMO/Ir cell, b) Impedance complex plane plot of Pt/Ir cell, c) Raw polarization curves and d) HFR-corrected Polarization curves of NiCu MMO/Ir and Pt/Ir cell in 1 and 0.1 M KOH.

and depressed semicircles. The ohmic resistance of the cell was determined from the high-frequency resistance (HFR), i.e., from the intercept with the real (*Re*) axes [87].

In Fig. 8, we show the equivalent circuit that is used to fit the impedance data taken at 0.2 A/cm^2 in both NiCu MMO and Pt/C cells. We assign the low-frequency arc to mass transport [87,88] and the high-frequency arc to electrode kinetics contributions to the cell voltage from the NiCu MMO and Pt/C cathodes. The fitted electrical circuit is comprised of a series combination of two parallel circuits each consisting of a resistance and a constant phase element (CPE), in series with a resistor, R_Ω. The R_Ω corresponds to the ohmic resistance of the cell (catalyst layer, current collectors and membrane). The R_{ct} describes the charge transfer resistance of the cathode and anode. CPE_1 is the constant phase element that represents the electrode roughness. The circuit has an additional RC combination, constant phase element, and the resistance (CPE_2 and R_1), which is suggested to describe the mass transport related to bubble formation at the electrode-electrolyte interface [88]. All parameters extracted from the fitting of the impedance data to are presented in Table S3. For 1 M KOH, NiCu MMO cell has an HFR of 0.195 Ω.cm^2 while Pt/C based AEMWE cell has an HFR of 0.115 Ω.cm^2. NiCu MMO cell displays an HFR of 0.295 Ω.cm^2 while Pt/C achieves 0.225 Ω.cm^2 in 0.1 M KOH. NiCu MMO (5 mg/cm^2) higher loadings resulted in thicker catalyst layers and higher HFR compared to Pt/C. The HFR increases as KOH concentration decreases to 0.1 M KOH. This HFR increase with decreasing KOH concentration may indicate insufficient ionic conductivity of the membrane [26].

The impedance data were converted to Tafel impedance. The Tafel slope can be estimated from the Tafel impedance, for a kinetically limited process, as the diameter of the impedance arc [89]. The Tafel impedance shown in Fig. S8 ESI† is the impedance multiplied with the steady-state current density at which it was obtained. We thus estimate the Tafel slope in 1 M KOH to be 40 mV for Pt and 65 mV for NiCu MMO at 0.2 A/cm^2. The Tafel slope from the impedance data is in the range of 50 millivolts, whereas the slopes from the polarization curve are twice this value (see Fig. S9 ESI) suggested that the polarization curves are dominated by the ohmic resistance. Fig. 8c and 8d show the potentiostatic polarization curves of both HFR-corrected and uncorrected voltages for the AEMWE at different KOH concentrations for NiCu MMO and Pt/C cells.

Fig. 8c and 8d show the AEM electrolyzer performance of NiCu MMO and Pt/C cathode catalysts in 1 and 0.1 M KOH at 50 °C using Ir black as an anode. In 1 M KOH, with NiCu MMO a cell performance of 1.85 A/cm^2 at 2 V achieved, which may be compared to Pt /Ir cell that delivers 2 A/cm^2 at 2 V in 1 M KOH while both cells achieved 1 A/cm^2 at 2 V in 0.1 M KOH. The increase in KOH electrolyte concentration leads to a higher AEM electrolyzer performance.

Fig. 8d showed that NiCu MMO cell exhibits higher performance than Pt/C catalyst when HFR-corrected. NiCu MMO (5 mg/cm^2)

shows higher resistance than Pt/C (1 mg/cm^2) in 1 and 0.1 M KOH (Fig. 8a and 8b). Since the cell hardware, components, electrolyte, temperature is the same and the only difference is the cathode catalyst, the origin of high resistance is the higher loading and the presence of oxide species in NiCu MMO (Ni-NiO-CuO). This leads to a higher resistance in the NiCu MMO catalytic layer itself as compared to the Pt/C, with its lower loading and metallic conductivity.

The results suggest that the differences in the activity of the samples (Fig. 8c) are not merely due to their different intrinsic activities, but also partly due to low electronic resistance in the catalytic layer. This contribution to the resistance will be particularly significant for poorly conducting oxides such as those of NiCu MMO. The high-frequency resistance (HFR) corrected polarization curves in Fig. 8d confirm that the electronic resistance of the cathode catalyst layer significantly affects cell performance. Similar results can be found in the literature. Yu et al. [90] showed that for catalysts with widely different conductivity the ranking depends on whether iR compensation is applied or not. Xu et al. [91] referred the differences in AEM electrolyzer performance partially to differences in the OER catalyst phases electrical conductivity. Finally, D. Chung et al. [92] showed that poorly conductive MoS_2 HER activity is affected by the ohmic losses and recommend that electrical conductivity should be considered when designing active catalysts for water electrolysis.

The NiCu MMO/Ir MEA activity shows a good reproducibility for three different MEAs in 1 M KOH at 50 °C as in Fig. S10 ESI†. The post-mortem analysis of NiCu MMO catalytic layers shows no visible cracks which prove the stability of catalytic layers during AEM water electrolysis as indicated in Fig. S11. Energy dispersive X-ray (EDX) mapping of NiCu MMO catalytic layers and cross-section shows the presence of nickel, copper, carbon, and a thin potassium layer after the electrolysis experiment Fig. S12, and S13 ESI†.

The excellent performance of 1.85 A/cm^2 at 2 V in 1 M KOH obtained for the NiCu MMO hydrogen catalyst outperforms most of those summarized in (Fig. S14 and Table S4 ESI†) allows for an active and cheap catalyst for AEM water electrolysis operation on a commercial scale [93,94] and comparable to the state of the art performance of PEM electrolysis as summarized by Ayers et al. [95].

Conclusions

NiCu mixed metal oxide (MMO) nanosheets synthesized by chemical reduction showed an exceptional activity for the HER compared to NiCu alloy and NiCu oxide catalysts, with higher performance in 1 M KOH than 0.1 M KOH. The improved HER kinetics of the NiCu MMO bifunctional system can be attributed to the presence of both Ni and NiO where NiO sites to facilitate water dissociation and bind OH_{ad} while Ni metallic binds H_{ads} and CuO stabilizes NiO under HER conditions. In situ Raman spectroscopy at the NiCu MMO catalysts showed that a substantial fraction of in situ formed nickel hydroxide remained after 30,000 s at HER conditions, which may explain why the NiCu MMO is able to maintain its very high activity as compared to that of NiCu alloy and NiCu oxide over longer periods of time. Despite that anion exchange ionomers would be expected to be suitable ionomers in an AEM environment, the application of anion exchange ionomers in catalytic layers resulted in a lower HER activity as compared to catalytic layers with Nafion as the ionomer. Using Ir black as an anode catalyst, cells with NiCu MMO nanosheets as cathode catalyst achieved AEM electrolyzer performance of 1.85 A/cm^2 at 2 V in 1 M KOH at 50 °C.

Declaration of Competing Interest

"There are no conflicts to declare."

Credit authorship contribution statement

Alaa Y. Faid: Conceptualization, Methodology, Investigation, Writing - original draft, Writing - review & editing. **Alejandro Oyarce Barnett:** Funding acquisition, Supervision, Writing - review & editing. **Frode Seland:** Supervision, Writing - review & editing. **Svein Sunde:** Funding acquisition, Supervision, Writing - review & editing.

Acknowledgments

This work was performed within HAPEEL project "Hydrogen Production by Alkaline Polymer Electrolyte Electrolysis" financially supported by the Research Council of Norway-ENERGIX program contract number 268019 and the INTPART project 261620. The Research Council of Norway is acknowledged for the support to the Norwegian Micro- and Nano-Fabrication Facility, NorFab, project number 245963/F50.

Supplementary materials

Supplementary material associated with this article can be found, in the online version, at doi:10.1016/j.electacta.2021.137837.

References

[1] A.Y Faid, A. Oyarce Barnett, F. Seland, S. Sunde, A.Y. Faid, A. Oyarce Barnett, F. Seland, S. Sunde, Highly active nickel-based catalyst for hydrogen evolution in anion exchange membrane electrolysis, Catalysts 8 (12) (2018) 614, doi:10.3390/catal8120614.
[2] I. Vincent, D. Bessarabov, Low cost hydrogen production by anion exchange membrane electrolysis : a review, Renew. Sustain. Energy Rev. 81 (May) (2017) 1–15, doi:10.1016/j.rser.2017.05.258.
[3] J.R. Varcoe, P. Atanassov, D.R. Dekel, A.M. Herring, M.A. Hickner, P.A. Kohl, A.R. Kucernak, W.E. Mustain, K. Nijmeijer, K. Scott, T. Xu, L. Zhuang, Anion-exchange membranes in electrochemical energy systems, Energy Environ. Sci. 7 (10) (2014) 3135–3191, doi:10.1039/C4EE01303D.
[4] A.Y. Faid, A.O. Barnett, F. Seland, S. Sunde, Optimized nickel-cobalt and nickel-iron oxide catalysts for the hydrogen evolution reaction in alkaline water electrolysis, J. Electrochem. Soc. 166 (8) (2019) F519–F533, doi:10.1149/2.0821908jes.
[5] X. Zou, Y. Zhang, Noble metal-free hydrogen evolution catalysts for water splitting, Chem. Soc. Rev. 44 (15) (2015) 5148–5180, doi:10.1039/C4CS00448E.
[6] M. Bodner, A. Hofer, V. Hacker, H_2 Generation from alkaline electrolyzer, Wiley Interdiscip. Rev. Energy Environ. 4 (4) (2015) 365–381, doi:10.1002/wene.150.
[7] A.R. Zeradjanin, J.P. Grote, G. Polymeros, K.J.J. Mayrhofer, A critical review on hydrogen evolution electrocatalysis: *re*-exploring the volcano-relationship, Electroanalysis 28 (10) (2016) 2256–2269, doi:10.1002/elan.201600270.
[8] F. Safizadeh, E. Ghali, G. Houlachi, Electrocatalysis developments for hydrogen evolution reaction in alkaline solutions - a review, Int. J. Hydrog. Energy 40 (1) (2015) 256–274, doi:10.1016/j.ijhydene.2014.10.109.
[9] N. Mahmood, Y. Yao, J.W. Zhang, L. Pan, X. Zhang, J.J. Zou, Electrocatalysts for hydrogen evolution in alkaline electrolytes: mechanisms, challenges, and prospective solutions, Advanced Science, Wiley-VCH Verlag, February 1, 2018, doi:10.1002/advs.201700464.
[10] Y. Zheng, Y. Jiao, S.S. Qiao, A. Vasileff, S.S. Qiao, A. Vasileff, Hydrogen evolution reaction in alkaline solution: from theory, single crystal models, to practical electrocatalysts, Angew. Chem. Int. Ed. (2017) 2–14, doi:10.1002/anie.201710556.
[11] T. Shinagawa, A.T. Garcia-Esparza, K. Takanabe, Insight on Tafel slopes from a microkinetic analysis of aqueous electrocatalysis for energy conversion, Sci. Rep. 5 (September) (2015) 1–21, doi:10.1038/srep13801.
[12] J. He, L. Zu, X. Liu, L. Zhang, B. Duan, Porous NiCu alloy cathode with oriented pore structure for hydrogen evolution reaction by freeze casting, J. Porous Mater. (0123456789) (2019), doi:10.1007/s10934-019-00751-9.
[13] D.S.P. Cardoso, S. Eugénio, T.M. Silva, D.M.F. Santos, C.A.C. Sequeira, M.F. Montemor, Hydrogen evolution on nanostructured Ni-Cu foams, RSC Adv. 5 (54) (2015) 43456–43461, doi:10.1039/c5ra06517h.
[14] K. Wang, M. Xia, T. Xiao, T. Lei, W. Yan, Metallurgically prepared NiCu alloys as cathode materials for hydrogen evolution reaction, Mater. Chem. Phys. 186 (2017) 61–66, doi:10.1016/j.matchemphys.2016.10.029.
[15] X. He, F. Di; Xu, F. Li, L. Liu, Y. Wang, N. Deng, Y.W. Zhu, J.B. He, Composition-performance relationship of NixCuy nanoalloys as hydrogen evolution electrocatalyst, J. Electroanal. Chem. 799 (April) (2017) 235–241, doi:10.1016/j.jelechem.2017.05.050.
[16] M.Y. Gao, C. Yang, Q.B. Zhang, Y.W. Yu, Y.X. Hua, Y. Li, P. Dong, Electrochemical fabrication of porous Ni-Cu alloy nanosheets with high catalytic activity for hydrogen evolution, Electrochim. Acta 215 (2016) 609–616, doi:10.1016/j.electacta.2016.08.145.

[17] R. Solmaz, A. Döner, G. Kardaş, The stability of hydrogen evolution activity and corrosion behavior of NiCu coatings with long-term electrolysis in alkaline solution, Int. J. Hydrog. Energy 34 (5) (2009) 2089–2094, doi:10.1016/j.ijhydene.2009.01.007.

[18] R. Solmaz, A. Döner, G. Kardaş, Preparation, characterization and application of alkaline leached CuNiZn ternary coatings for long-term electrolysis in alkaline solution, Int. J. Hydrog. Energy 35 (19) (2010) 10045–10049, doi:10.1016/j.ijhydene.2010.07.145.

[19] A.G. Oshchepkov, P.A. Simonov, O.V. Cherstiouk, R.R. Nazmutdinov, D.V. Glukhov, V.I. Zaikovskii, T.Y. Kardash, R.I. Kvon, A. Bonnefont, A.N. Simonov, V.N. Parmon, E.R Savinova, On the effect of Cu on the activity of carbon supported ni nanoparticles for hydrogen electrode reactions in alkaline medium, Top. Catal. 58 (18–20) (2015) 1181–1192, doi:10.1007/s11244-015-0487-5.

[20] Y. Xie, X. Wang, K. Tang, Q. Li, C. Yan, Blending Fe_3O_4 into a Ni/NiO composite for efficient and stable bifunctional electrocatalyst, Electrochim. Acta 264 (2018) 225–232, doi:10.1016/j.electacta.2018.01.136.

[21] M.K. Bates, Q. Jia, N. Ramaswamy, R.J. Allen, S. Mukerjee, Composite Ni/NiO-Cr_2O_3 catalyst for alkaline hydrogen evolution reaction, J. Phys. Chem. C 119 (10) (2015) 5467–5477, doi:10.1021/jp512311c.

[22] M. Gong, W. Zhou, M.J. Kenney, R. Kapusta, S. Cowley, Y. Wu, B. Lu, M.C. Lin, D.Y. Wang, J. Yang, B.J. Hwang, H. Dai, Blending Cr_2O_3 into a NiO-Ni electrocatalyst for sustained water splitting, Angew. Chem. - Int. Ed. 54 (41) (2015) 11989–11993, doi:10.1002/anie.201504815.

[23] M. Gong, W. Zhou, M.C. Tsai, J. Zhou, M. Guan, M.C. Lin, B. Zhang, Y. Hu, D.Y. Wang, J. Yang, S.J. Pennycook, B.J. Hwang, H. Dai, Nanoscale nickel oxide/nickel heterostructures for active hydrogen evolution electrocatalysis, Nat. Commun. 5 (2014) 1–6, doi:10.1038/ncomms5695.

[24] R. Jervis, N. Mansor, A.J. Sobrido, S. Jones, C. Gibbs, T.P. Neville, J. Millichamp, P.R. Shearing, D.J.L Brett, The importance of using alkaline ionomer binders for screening electrocatalysts in alkaline electrolyte, J. Electrochem. Soc. 164 (14) (2017) F1551–F1555, doi:10.1149/2.0441714jes.

[25] S.M. Alia, B.S. Pivovar, Evaluating hydrogen evolution and oxidation in alkaline media to establish baselines, J. Electrochem. Soc. 165 (7) (2018) F441–F455, doi:10.1149/2.0361807jes.

[26] L. Trotochaud, S.L. Young, J.K. Ranney, S.W. Boettcher, Nickel-iron oxyhydroxide oxygen-evolution electrocatalysts: the role of intentional and incidental iron incorporation, J. Am. Chem. Soc. 136 (18) (2014) 6744–6753, doi:10.1021/ja502379c.

[27] Y. Deng, B.S. Yeo, Characterization of electrocatalytic water splitting and CO2 reduction reactions using in situ/operando raman spectroscopy, ACS Catal (2017) 7873–7889, doi:10.1021/acscatal.7b02561.

[28] A.Y. Faid, A.O. Barnett, F. Seland, S. Sunde, Ni/NiO nanosheets for alkaline hydrogen evolution reaction: in situ electrochemical-Raman study, Electrochim. Acta 361 (2020) 137040, doi:10.1016/j.electacta.2020.137040.

[29] S. Wang, P. He, Z. Xie, L. Jia, M. He, X. Zhang, F. Dong, H. Liu, Y. Zhang, C. Li, Tunable nanocotton-like amorphous ternary Ni-Co-B: a highly efficient catalyst for enhanced oxygen evolution reaction, Electrochim. Acta 296 (2019) 644–652, doi:10.1016/j.electacta.2018.11.099.

[30] C. Zhu, D. Wen, S. Leubner, M. Oschatz, W. Liu, M. Holzschuh, F. Simon, S. Kaskel, A. Eychmüller, Nickel cobalt oxide hollow nanosponges as advanced electrocatalysts for the oxygen evolution reaction, Chem. Commun. 51 (37) (2015) 7851–7854, doi:10.1039/c5cc01558h.

[31] S. Fu, C. Zhu, J. Song, M.H. Engelhard, Y. He, D. Du, C. Wang, Y. Lin, Three-dimensional PtNi hollow nanochains as an enhanced electrocatalyst for the oxygen reduction reaction, J. Mater. Chem. A 4 (22) (2016) 8755–8761, doi:10.1039/c6ta01801g.

[32] Q. Lu, J. Huang, C. Han, L. Sun, X. Yang, Facile synthesis of composition-tunable ptrh nanosponges for methanol oxidation reaction, Electrochim. Acta 266 (2018) 305–311, doi:10.1016/j.electacta.2018.02.021.

[33] Y. Jiang, Y. Fang, C. Chen, P. Ni, B. Kong, Z. Song, Y. Lu, L. Niu, Amorphous cobalt boride nanosheets directly grown on nickel foam: controllable alternately dipping deposition for efficient oxygen evolution, ChemElectroChem 6 (14) (2019) 3684–3689, doi:10.1002/celc.201900897.

[34] J. Masa, I. Sinev, H. Mistry, E. Ventosa, M. de la Mata, J. Arbiol, M. Muhler, B. Roldan Cuenya, W. Schuhmann, Ultrathin high surface area nickel boride (NixB) nanosheets as highly efficient electrocatalyst for oxygen evolution, Adv. Energy Mater. 7 (17) (2017) 1–8, doi:10.1002/aenm.201700381.

[35] X. Chen, Z. Yu, L. Wei, Z. Zhou, S. Zhai, J. Chen, Y. Wang, Q. Huang, H. Enis Karahan, X. Liao, Y. Chen, Ultrathin nickel boride nanosheets anchored on functionalized carbon nanotubes as bifunctional electrocatalysts for overall water splitting, J. Mater. Chem. A 7 (2) (2019) 764–774, doi:10.1039/c8ta09130g.

[36] H. Sun, X. Xu, Z. Yan, X. Chen, L. Jiao, F. Cheng, J. Chen, Superhydrophilic amorphous Co-B-P nanosheet electrocatalysts with Pt-like activity and durability for the hydrogen evolution reaction, J. Mater. Chem. A 6 (44) (2018) 22062–22069, doi:10.1039/C8TA02999G.

[37] J.M.V. Nsanzimana, V. Reddu, Y. Peng, Z. Huang, C. Wang, X Wang, Ultrathin amorphous iron–nickel boride nanosheets for highly efficient electrocatalytic oxygen production, Chem. - A Eur. J. 24 (69) (2018) 18502–18511, doi:10.1002/chem.201802092.

[38] T. He, J. Marie, V. Nsanzimana, R. Qi, J.Y. Zhang, M. Miao, Y. Yan, K. Qi, H. Liu, B.Y. Xia, J.M.V. Nsanzimana, R. Qi, J.Y. Zhang, M. Miao, Y. Yan, K. Qi, H. Liu, B.Y. Xia, Synthesis of amorphous boride nanosheets by the chemical reduction of prussian blue analogs for efficient water electrolysis, J. Mater. Chem. A 6 (46) (2018) 23289–23294, doi:10.1039/C8TA09609K.

[39] J. Marie, V. Nsanzimana, R. Dangol, V. Reddu, S. Duo, Y. Peng, K.N. Dinh, Z. Huang, Q. Yan, X. Wang, Facile synthesis of amorphous ternary metal borides – reduced graphene oxide hybrid with superior oxygen evolution activity, ACS Appl. Mater. Interfaces 11 (2018) 846–855, doi:10.1021/acsami.8b17836.

[40] Y. Yang, L. Zhuang, T.E. Rufford, S. Wang, Z. Zhu, Efficient water oxidation with amorphous transition metal boride catalysts synthesized by chemical reduction of metal nitrate salts at room temperature, RSC Adv. 7 (52) (2017) 32923–32930, doi:10.1039/c7ra02558k.

[41] K.S. Krishna, C.S.S. Sandeep, R. Philip, M. Eswaramoorthy, Mixing does the magic: a rapid synthesis of high surface area noble metal nanosponges showing broadband nonlinear optical response, ACS Nano 4 (5) (2010) 2681–2688, doi:10.1021/nn100320s.

[42] S. Gupta, M.K. Patel, A. Miotello, N. Patel, Metal boride-based catalysts for electrochemical water-splitting: a review, Adv. Funct. Mater. (2019) 1906481 *n/a* (n/a), doi:10.1002/adfm.201906481.

[43] R. Ding, J. Liu, J. Jiang, F. Wu, J. Zhu, X. Huang, Tailored Ni–Cu alloy hierarchical porous nanowire as a potential efficient catalyst for DMFCs, Catal. Sci. Technol. 1 (8) (2011) 1406, doi:10.1039/c1cy00164g.

[44] H. Yan, D. Zhang, J. Xu, Y. Lu, Y. Liu, K. Qiu, Y. Zhang, Y. Luo, Solution growth of NiO nanosheets supported on Ni foam as high-performance electrodes for supercapacitors, Nanoscale Res. Lett. 9 (1) (2014) 1–7, doi:10.1186/1556-276X-9-424.

[45] D. Manyasree, K.M. Peddi, R. Ravikumar, CuO nanoparticles: synthesis, characterization and their bactericidal efficacy, Int. J. Appl. Pharm. 9 (6) (2017) 71–74, doi:10.22159/ijap.2017v9i6.71757.

[46] G.H.M. Saeed, S. Radiman, S.S. Gasaymeh, H.N. Lim, N.M Huang, Mild hydrothermal synthesis of Ni-Cu nanoparticles, J. Nanomater. 2010 (2010) 5, doi:10.1155/2010/184137.

[47] Y. Deng, A.D. Handoko, Y. Du, S. Xi, B.S. Yeo, In situ Raman spectroscopy of copper and copper oxide surfaces during electrochemical oxygen evolution reaction: identification of CuIII oxides as catalytically active species, ACS Catal 6 (4) (2016) 2473–2481, doi:10.1021/acscatal.6b00205.

[48] M. Rashad, M. Rüsing, G. Berth, K. Lischka, A. Pawlis, CuO and Co_3O_4 nanoparticles: synthesis, characterizations, and Raman spectroscopy, J. Nanomater. 2013 (2013) 6, doi:10.1155/2013/714853.

[49] D. Kudryashov, A. Monastyrenko, A. Mozharov, A. Bukatin, E. Nikitina, E. Pirogov, A. Gudovskikh, Copper (I) oxide Rf-magnetron sputtering at elevated substrate temperatures, J. Phys. Conf. Ser. 917 (3) (2017) 0–5, doi:10.1088/1742-6596/917/3/032020.

[50] P. Sriyutha Murthy, V.P. Venugopalan, D. Das; Arunya, S. Dhara, R. Pandiyan, A.K. Tyagi, Antibiofilm activity of nano sized CuO, in: Proceeding International Conference on Nanoscience Engineering and Technology ICONSET 2011, 2011, pp. 580–583, doi:10.1109/ICONSET.2011.6168037. No. November.

[51] N. Mironova-Ulmane, A. Kuzmin, I. Steins, J. Grabis, I. Sildos, M. Pärs, Raman scattering in nanosized nickel oxide NiO, J. Phys. Conf. Ser. 93 (2007) 012039, doi:10.1088/1742-6596/93/1/012039.

[52] G. George, S. Anandhan, Synthesis and characterisation of nickel oxide nanofibre webs with alcohol sensing characteristics, RSC Adv 4 (107) (2014) 62009–62020, doi:10.1039/c4ra11083h.

[53] N. Mironova-Ulmane, A. Kuzmin, I. Sildos, M. Pärs, Polarisation dependent Raman study of single-crystal nickel oxide, Cent. Eur. J. Phys. 9 (4) (2011) 1096–1099, doi:10.2478/s11534-010-0130-9.

[54] V. Sathe, Improved electrochromic performance of a radio frequency magnetron sputtered NiO thin film with high optical switching speed, RSC Adv 6 (83) (2016) 79668–79680, doi:10.1039/C5RA27099E.

[55] W. Jia, Y. Chen, M. Liu, X. Liu, X. Liu, J. Yuan, X. Lu, Z. Zhu, Effect of calcination temperature and fluorination treatment on NiF2-AlF3 catalysts for dehydrofluorination of 1, 1, 1, 2-tetrafluoroethane to synthesize trifluoroethylene, Appl. Catal. A Gen. 571 (December) (2019) 150–157, doi:10.1016/j.apcata.2018.12.001.

[56] M. Chu, L. Wang, X. Li, M. Hou, N. Li, Y. Dong, X. Li, Z. Xie, Y. Lin, W. Cai, C. Zhang, Carbon coated nickel - nickel oxide composites as a highly efficient catalyst for hydrogen evolution reaction in acid medium, Electrochim. Acta 264 (2018) 284–291, doi:10.1016/j.electacta.2018.01.140.

[57] L. Sun, Y. Deng, Y. Yang, Z. Xu, K. Xie, L. Liao, Preparation and catalytic activity of magnetic bimetallic nickel/copper nanowires, RSC Adv 7 (29) (2017) 17781–17787, doi:10.1039/c7ra01068k.

[58] M.C. Biesinger, Advanced analysis of copper X-ray photoelectron spectra, Surf. Interface Anal. 49 (13) (2017) 1325–1334, doi:10.1002/sia.6239.

[59] M. Yu, W. Wang, C. Li, T. Zhai, X. Lu, Y. Tong, Scalable self-growth of Ni@NiO core-shell electrode with ultrahigh capacitance and super-long cyclic stability for supercapacitors, NPG Asia Mater. 6 (9) (2014) e129, doi:10.1038/am.2014.78.

[60] M.A. Peck, M.A. Langell, Comparison of nanoscaled and bulk NiO structural and environmental characteristics by XRD, XAFS, and XPS, Chem. Mater. 24 (23) (2012) 4483–4490, doi:10.1021/cm300739y.

[61] L. Zhu, H. Li, Z. Liu, P. Xia, Y. Xie, D. Xiong, Synthesis of the 0D/3D CuO/ZnO heterojunction with enhanced photocatalytic activity, J. Phys. Chem. C 122 (17) (2018) 9531–9539, doi:10.1021/acs.jpcc.8b01933.

[62] N. Danilovic, R. Subbaraman, D. Strmcnik, K.C. Chang, A.P. Paulikas, V.R. Stamenkovic, N.M. Markovic, Enhancing the alkaline hydrogen evolution reaction activity through the bifunctionality of $Ni(OH)_2$/metal catalysts, Angew. Chemie - Int. Ed. 51 (50) (2012) 12495–12498, doi:10.1002/anie.201204842.

[63] O. Diaz-Morales, D. Ferrus-Suspedra, M.T.M Koper, The importance of nickel oxyhydroxide deprotonation on its activity towards electrochemical water oxidation, Chem. Sci. 7 (4) (2016) 2639–2645, doi:10.1039/C5SC04486C.

[64] T. Zhang, X. Liu, X. Cui, M. Chen, S. Liu, B. Geng, Colloidal synthesis of Mo – Ni alloy nanoparticles as bifunctional electrocatalysts for efficient overall water splitting, Adv. Mater. Interfaces 1800359 (13) (2018) 1–6, doi:10.1002/admi.201800359.
[65] A. Lasia, Mechanism and kinetics of the hydrogen evolution reaction, Int. J. Hydrog. Energy 44 (36) (2019) 19484–19518, doi:10.1016/j.ijhydene.2019.05.183.
[66] H. Dong, T. Lei, Y. He, N. Xu, B. Huang, C.T. Liu, Electrochemical performance of porous Ni_3 Al electrodes for hydrogen evolution reaction, Int. J. Hydrogen Energy 36 (19) (2011) 12112–12120, doi:10.1016/j.ijhydene.2011.06.115.
[67] J.O.M.M. Bockris, E.C Potter, The mechanism of hydrogen evolution at nickel cathodes in aqueous solutions, J. Chem. Phys. 20 (4) (1952) 614–628, doi:10.1063/1.1700503.
[68] X. Wang, C. Xu, M. Jaroniec, Y. Zheng, S.Z. Qiao, Anomalous hydrogen evolution behavior in high-pH environment induced by locally generated hydronium ions, Nat. Commun. 10 (1) (2019) 1–8, doi:10.1038/s41467-019-12773-7.
[69] J. Kibsgaard, I. Chorkendorff, Considerations for the scaling-up of water splitting catalysts, Nat. Energy 4 (6) (2019) 430–433, doi:10.1038/s41560-019-0407-1.
[70] L. Zhang, K. Xiong, Y. Nie, X. Wang, J. Liao, Z. Wei, Sputtering nickel-molybdenum nanorods as an excellent hydrogen evolution reaction catalyst, J. Power Sources 297 (2015) 413–418, doi:10.1016/j.jpowsour.2015.08.004.
[71] Y. Zhang, Y. Wang, S. Jia, H. Xu, J. Zang, J. Lu, X. Xu, A hybrid of NiMo-Mo_2C/C as non-noble metal electrocatalyst for hydrogen evolution reaction in an acidic solution, Electrochim. Acta 222 (2016) 747–754, doi:10.1016/j.electacta.2016.11.031.
[72] X. Shang, J.Q. Chi, Z.Z. Liu, B. Dong, K.L. Yan, W.K. Gao, J. Zeng, Y.M. Bin; Chai, C.G. Liu, Ternary Ni-Fe-V sulfides bundles on nickel foam as free-standing hydrogen evolution electrodes in alkaline medium, Electrochim. Acta 256 (2017) 241–251, doi:10.1016/j.electacta.2017.10.050.
[73] T. Rauscher, C.I. Müller, A. Schmidt, B. Kieback, L. Röntzsch, Ni-Mo-B alloys as cathode material for alkaline water electrolysis, Int. J. Hydrog. Energy 41 (4) (2016) 2165–2176, doi:10.1016/j.ijhydene.2015.12.132.
[74] D. Merki, H. Vrubel, L. Rovelli, S. Fierro, X. Hu, Fe, Co, and Ni ions promote the catalytic activity of amorphous molybdenum sulfide films for hydrogen evolution, Chem. Sci. 3 (8) (2012) 2515, doi:10.1039/c2sc20539d.
[75] M.W. Louie, A.T. Bell, An investigation of thin-film Ni-Fe oxide catalysts for the electrochemical evolution of oxygen, J. Am. Chem. Soc. 135 (33) (2013) 12329–12337, doi:10.1021/ja405351s.
[76] Y. Ma, W. Yan, Q. Sun, X. Liu, Raman and infrared spectroscopic quantification of the carbonate concentration in K_2CO_3 aqueous solutions with water as an internal standard, Geosci. Front. (2020), doi:10.1016/j.gsf.2020.03.002.
[77] M. Peña-Álvarez, E. Corro, F. Del; Langa, V.G. Baonza, M. Taravillo, Morphological changes in carbon nanohorns under stress: a combined Raman spectroscopy and TEM study, RSC Adv. 6 (55) (2016) 49543–49550, doi:10.1039/c5ra27162b.
[78] S.A. Chernyak, A.S. Ivanov, K.I. Maslakov, A.V. Egorov, Z. Shen, S.S. Savilov, V.V.Oxidation Lunin, Defunctionalization and catalyst life cycle of carbon nanotubes: a Raman spectroscopy view, Phys. Chem. Chem. Phys. 19 (3) (2017) 2276–2285, doi:10.1039/c6cp04657f.
[79] R.W. Revie, Uhlig's Corrosion Handbook: Third Edition, John Wiley and Sons, 2011, doi:10.1002/9780470872864.
[80] N. Danilovic, R. Subbaraman, D. Strmcnik, K.-.C. Chang, A.P. Paulikas, V.R. Stamenkovic, N.M. Markovic, Enhancing the alkaline hydrogen evolution reaction activity through the bifunctionality of $Ni(OH)_2$ /metal catalysts, Angew. Chem. 124 (50) (2012) 12663–12666, doi:10.1002/ange.201204842.
[81] Y. Miao, L. Ouyang, S. Zhou, L. Xu, Z. Yang, M. Xiao, R. Ouyang, Electrocatalysis and electroanalysis of nickel, its oxides, hydroxides and oxyhydroxides toward small molecules, Biosens. Bioelectron. 53 (2014) 428–439, doi:10.1016/j.bios.2013.10.008.
[82] M.K. Bates, Q. Jia, N. Ramaswamy, R.J. Allen, S. Mukerjee, Composite Ni/NiO-Cr_2O_3 catalyst for alkaline hydrogen evolution reaction, J. Phys. Chem. C 119 (10) (2015) 5467–5477, doi:10.1021/jp512311c.
[83] N. Daems, T. Breugelmans, I.F.J. Vankelecom, P.P. Pescarmona, Influence of the composition and preparation of the rotating disk electrode on the performance of mesoporous electrocatalysts in the alkaline oxygen reduction reaction, ChemElectroChem 5 (1) (2018) 119–128, doi:10.1002/celc.201700907.
[84] A.Y. Faid, L. Xie, A.O. Barnett, F. Seland, D. Kirk, S. Sunde, Effect of anion exchange ionomer content on electrode performance in AEM water electrolysis, Int. J. Hydrog. Energy 45 (53) (2020) 28272–28284, doi:10.1016/j.ijhydene.2020.07.202.
[85] H.T. Chung, U. Martinez, I. Matanovic, Y.S. Kim, Cation-hydroxide-water coadsorption inhibits the alkaline hydrogen oxidation reaction, J. Phys. Chem. Lett. 7 (22) (2016) 4464–4469, doi:10.1021/acs.jpclett.6b02025.
[86] G.F. Li, D. Yang, P.Y. Abel Chuang, Defining nafion ionomer roles for enhancing alkaline oxygen evolution electrocatalysis, ACS Catal. (2018) 11688–11698, doi:10.1021/acscatal.8b02217.
[87] S. Sun, Z. Shao, H. Yu, G. Li, B. Yi, Investigations on degradation of the long-term proton exchange membrane water electrolysis stack, J. Power Sources 267 (2014) 515–520, doi:10.1016/j.jpowsour.2014.05.117.
[88] I. Dedigama, P. Angeli, K. Ayers, J.B. Robinson, P.R. Shearing, D. Tsaoulidis, D.J.L. Brett, In situ diagnostic techniques for characterisation of polymer electrolyte membrane water electrolysers - flow visualisation and electrochemical impedance spectroscopy, Int. J. Hydrog. Energy 39 (9) (2014) 4468–4482, doi:10.1016/j.ijhydene.2014.01.026.
[89] F. Jaouen, G. Lindbergh, Transient techniques for investigating mass-transport limitations in gas diffusion electrodes, J. Electrochem. Soc. 150 (12) (2003), doi:10.1149/1.1624294.
[90] L. Yu, Z. Ren, Systematic study of the influence of IR compensation on water electrolysis, Mater. Today Phys. 14 (2020) 100253, doi:10.1016/j.mtphys.2020.100253.
[91] D. Xu, M.B. Stevens, M.R. Cosby, S.Z. Oener, A.M. Smith, L.J. Enman, K.E. Ayers, C.B. Capuano, J.N. Renner, N. Danilovic, Y. Li, H. Wang, Q. Zhang, S.W. Boettcher, Earth-abundant oxygen electrocatalysts for alkaline anion-exchange-membrane water electrolysis: effects of catalyst conductivity and comparison with performance in three-electrode cells, ACS Catal 9 (1) (2019) 7–15, doi:10.1021/acscatal.8b04001.
[92] D.Y. Chung, S. Park, P.P. Lopes, V.R. Stamenkovic, Y.-.E. Sung, N.M. Markovic, D. Strmcnik, Electrokinetic analysis of poorly conductive electrocatalytic materials, ACS Catal. 10 (9) (2020) 4990–4996, doi:10.1021/acscatal.0c00960.
[93] A. Buttler, H. Spliethoff, Current status of water electrolysis for energy storage, grid balancing and sector coupling via power-to-gas and power-to-liquids: a review, Renew. Sustain. Energy Rev. 82 (September) (2018) 2440–2454, doi:10.1016/j.rser.2017.09.003.
[94] I. Vincent, D. Bessarabov, Low cost hydrogen production by anion exchange membrane electrolysis: a review, Renew. Sustain. Energy Rev. 81 (May) (2018) 1690–1704, doi:10.1016/j.rser.2017.05.258.
[95] K. Ayers, N. Danilovic, R. Ouimet, M. Carmo, B. Pivovar, M. Bornstein, Perspectives on low-temperature electrolysis and potential for renewable hydrogen at scale, Annu. Rev. Chem. Biomol. Eng. 10 (1) (2019) 219–239, doi:10.1146/annurev-chembioeng-060718-030241.